Metastasis and immune evasion from extracellular cGAMP hydrolysis

Jun Li[1,2,*], Mercedes A. Duran[1,2,*], Ninjit Dhanota[1,2], Walid Chatila[1,3], John Kwon[1,2], Roshan K Sriram[4], Matthew P Humphries[5], Manuel Salto-Tellez[5,6], Jacqueline A. James[5], Matthew Hanna[7], Johannes C. Melms[8,9], Sreeram Vallabhaneni[10], Kevin Litchfield[11], M. Laura Martin[12], Princesca Dorsaint[12], Julie-Ann Cavallo[1,2], Peng Li[13], Chantal Pauli[14], Lee Gottesdiener[15], Benjamin J. DiPardo[16], Travis Hollmann[7], Taha Merghoub[1,15,18-20], Hannah Wen[7], Jorge S. Reis-Filho[7], Nadeem Riaz[2], Anusha Kalbasi[17], Neil Vasan[15,18], Jedd D. Wolchok[1,15,18-20], Olivier Elemento[12], Charles Swanton[11], Alexander N. Shoushtari[15,18], Benjamin Izar[8,9,21,$], Eileen E. Parkes[5,6,$], Samuel F. Bakhoum[1,2,#]

[1] Human Oncology and Pathogenesis Program, Memorial Sloan Kettering Cancer Center, New York, NY
[2] Department of Radiation Oncology, Memorial Sloan Kettering Cancer Center, New York, NY
[3] Tri-Institutional Program in Computational Biology and Medicine, Weill Cornell Medical College, New York, NY
[4] Meyer Cancer Center, Weill Cornell Medicine, New York, NY
[5] Precision Medicine Centre of Excellence, Centre for Cancer Research and Cell Biology, Queen's University Belfast, Belfast, UK
[6] Department of Oncology, Medical Sciences Division, University of Oxford, Oxford, UK
[7] Department of Pathology, Memorial Sloan Kettering Cancer Center, New York, NY
[8] Columbia Center for Translational Immunology, New York, NY
[9] Columbia University Medical Center, Division of Hematology and Oncology, New York, NY
[10] Laboratory for Systems Pharmacology, Harvard Medical School, Boston, MA
[11] Cancer Evolution and Genome Instability Laboratory, The Francis-Crick Institute, London, UK
[12] Englander Institute for Precision Medicine, Meyer Cancer Center, Weill Cornell Medicine
[13] Immunology Program, Memorial Sloan Kettering Cancer Center, New York, NY
[14] Institute for Pathology and Molecular Pathology, University Hospital Zurich, Zurich 8091, Switzerland
[15] Department of Medicine, Memorial Sloan Kettering Cancer Center, New York, NY
[16] Department of Surgery, University of California, Los Angeles, CA 90095
[17] Department of Radiation Oncology, Jonsson Comprehensive Cancer Center, University of California, Los Angeles, CA 90095
[18] Department of Medicine, Weill Cornell Medicine, New York, NY
[19] Ludwig Collaborative and Swim Across America Laboratory, Memorial Sloan Kettering Cancer Center, New York, NY
[20] Parker Institute for Cancer Immunotherapy, Memorial Sloan Kettering Cancer Center, New York, NY 10065, USA.
[21] Broad Institute of MIT and Harvard, Cambridge, MA
[*] These authors contributed equally to this work
[$] These authors contributed equally to this work

Corresponding author:
Samuel F. Bakhoum, M.D., Ph.D.
Human Oncology and Pathogenesis Program
Department of Radiation Oncology
Memorial Sloan Kettering Cancer Center
New York, N.Y., 10065
Email: bakhoums@mskcc.org
Phone: 212-639-5749

Cytosolic DNA is characteristic of metastatic and chromosomally unstable cancer cells and it results in constitutive activation of the cGAS-STING innate immune pathway. How cancer cells co-opt inflammatory signaling while evading immune surveillance remains unknown. Here we show that the ectonucleotidase ENPP1 promotes metastasis by selectively degrading extracellular cGAMP, an immune stimulatory metabolite whose breakdown products include the immune suppressor, adenosine. ENPP1 depletion restores tumor immune infiltration, suppresses metastasis, and potentiates tumor response to immune checkpoint blockade (ICB) therapy. Conversely, its overexpression renders otherwise sensitive tumors completely resistant to ICB. In human cancers, ENPP1 expression correlates with reduced immune cell infiltration, increased metastasis, and resistance to anti-PD1/PD-L1 therapy. Thus, cGAMP hydrolysis by ENPP1 enables metastatic cancer cells to transmute an immune stimulatory pathway into an immune suppressive mechanism supporting tumor progression.

Chromosomal instability (CIN) is a hallmark of human cancer and it is associated with metastasis, immune evasion, and therapeutic resistance[1-5]. Chromosome segregation errors lead to the formation of micronuclei[6,7]. Micronuclear envelopes are highly rupture-prone, often exposing genomic double-stranded DNA (dsDNA) to the cytosol[7-12]. Cytosolic dsDNA is sensed by cGAS, which upon binding to its substrate, catalyzes the formation of the cyclic dinucleotide, cGAMP[13]. cGAMP is a potent immune-stimulatory molecule that promotes inflammatory signaling in a manner dependent on its downstream effector STING[14,15]. Chromosomally unstable cancer cells have evolved to cope with chronic cGAS-STING activation by silencing downstream type I interferon signaling whilst co-opting NF-κB-dependent transcription to spread to distant organs[9]. However, cGAMP is also readily exported to the extracellular space where it can promote anti-tumor immune responses by activating STING in neighboring host cells[16-18]. How aggressive cancer cells with CIN co-opt inflammatory signaling while simultaneously evading immune surveillance remains unknown.

To address this question, we used two syngeneic mouse models of triple-negative breast cancer (TNBC) metastasis (4T1) and colorectal cancer metastasis (CT26). As expected, both models exhibited high levels of CIN, as evidenced by the presence of chromosome missegregation during anaphase and a preponderance of micronuclei with robust cGAS localization (**Extended Data Fig. 1A-B**). cGAMP was readily detectable in total 4T1 cell lysates and CRISPR-Cas9 mediated knockout of *Cgas* resulted in a significant reduction in the levels of this metabolite (**Extended Data Fig. 1C-D**). Furthermore, cGAMP levels were nearly 15-fold higher in conditioned media after 24hr, as compared to cell lysates, when both were normalized to cell counts (**Extended Data Fig. 1E**), suggesting that cGAMP is readily exported from cancer cells, as previously proposed[16-18].

To determine how chromosomally unstable cells cope with ongoing cGAMP production, we made use of otherwise isogenic human MDA-MB-231 TNBC cells that were engineered to exhibit different rates of CIN through overexpression of the kinesin-13 proteins, Kif2b or MCAK, or the dominant-negative mutant isoform of MCAK (dnMCAK)[9,19]. Pairwise differential expression analysis comparing CIN^{high} (highly metastatic) to CIN^{low} (poorly metastatic) cells revealed a large number of differentially expressed genes, among which *ENPP1* stood out (**Extended Data Fig. 2A**, Log_2 fold change = 1.23, FDRq = $8.4x10^{-4}$) because of its role as an ectonucleotidase that hydrolyses cGAMP in the extracellular space[17,20]. Protein levels of ENPP1

were markedly increased in CIN^{high} cells compared with their CIN^{low} counterparts and staining using an anti-ENPP1 antibody revealed strong membrane localization that was abolished upon shRNA-mediated depletion (**Fig. 1A and Extended Data Fig. 2B-D**). Similar to our findings in human metastatic MDA-MB-231 cells, there was a significant increase in *ENPP1* messenger RNA (mRNA) levels in mouse lung metastasis-derived 4T1 cells as compared with the parental cell line (**Extended Data Fig. 2E**). And, even within orthotopically transplanted tumors, increased expression of ENPP1 was observed selectively in tumor cells invading nearby intra-mammary lymph nodes (**Fig. 1B**), suggesting that ENPP1 might play a role in promoting metastasis in chromosomally unstable cells.

To evaluate the role of ENPP1 in metastasis in an immune-competent setting, we performed CRISPR-Cas9 knockout (KO) of *Enpp1* in 4T1 cells (**Extended Data Fig. 2F**). As expected, loss of ENPP1 led to a significant increase in the extracellular-to-intracellular cGAMP ratio (**Fig. 1C**). We then transplanted parental and *Enpp1*-KO 4T1 cells into BALB/c hosts either through tail vein inoculation or orthotopic transplantation into the mammary fat pad followed by primary tumor excision. *Enpp1*-KO did not impact cellular proliferation *in vitro* or primary tumor growth *in vivo* when cells were orthotopically transplanted in the mammary fat pad (**Extended Data Fig. 2G-H**). However, loss of ENPP1 led to significantly longer overall survival and a marked reduction in local tumor recurrence and metastasis regardless of whether cells were introduced directly into the tail vein or orthotopically transplanted followed by surgical excision of the primary tumor (**Fig. 1D-E and Extended Data Fig. 2I-L**). These results suggest that disrupting the ability of chromosomally unstable cancer cells to sequester cGAS-STING signaling, by increasing extracellular cGAMP availability, might suppress metastatic progression.

To further explore the fate of tumor-derived extracellular cGAMP, we asked whether the breakdown products of this metabolite might contribute to the production of adenosine, an immune-suppressive and tumor-promoting molecule (**Fig. 2A-B**). Measuring adenosine in conditioned media is technically challenging given the presence of enzymes that either degrade this nucleoside (adenosine deaminase, ADA) or promote its cellular reuptake (**Extended Data Fig. 3A**). To overcome these challenges, we added serum-free media to 4T1 cells in the presence of erythro-9-(2-hydroxy-3-nonyl)adenine (EHNA), an ADA inhibitor, along with dipyridamole and 6-*S*-[(4-Nitrophenyl)methyl]-6-thioinosine (NBMPR), which prevent cellular reuptake of adenosine (**Extended Data Fig. 3A**)[21]. Extracellular adenosine levels – as assessed by liquid chromatography-mass spectrometry in conditioned media – were reduced by up to 40% upon knockout of either *Cgas* or *Enpp1* (**Fig. 2C**). Using an orthogonal approach, we added exogenous cGAMP to 4T1 cells and used a fluorescence-based method to detect hydrogen peroxide (H_2O_2) resulting from the oxidation of hypoxanthine, a breakdown product of adenosine (**Extended Data Fig. 3A**). By comparing fluorescence in the presence and absence of EHNA, we were able to assess relative contribution from adenosine degradation toward H_2O_2 production and observed a concentration-dependent increase in H_2O_2 production after the addition of exogenous addition of cGAMP (**Extended Data Fig. 3B**), suggesting that this cyclic dinucleotide can be readily converted into adenosine in the extracellular environment.

Through its ability to bind extracellular adenosine receptors in both tumor and immune cells, adenosine promotes cancer cell migration and is a potent immune suppressor, respectively (**Fig. 2B**)[22,23]. Interestingly, knockout of either *Cgas* or *Enpp1* led to a significant reduction in cancer cell migration, whereas exogenous addition of cGAMP rescued migration only in

Cgas-KO but not *Enpp1*-KO tumour cells (**Fig. 2D**). The effect of cGAMP was dependent on adenosine receptor activity and was abolished upon the addition of PSB115, an inhibitor of the adenosine A2B receptor on cancer cells (**Fig. 2D**).

We next examined the effect of ENPP1 loss on tumor immune infiltration using shRNA-mediated depletion or CRISPR-Cas9-mediated knockout in CIN^{high} MDA-MB-231 orthotopic xenografts and 4T1 allografts, respectively. Loss of ENPP1 led to increased tumor necrosis and enhanced infiltration of natural killer (NK)-cells in MDA-MB-231 tumors (**Extended Data Fig. 4A-B**), in line with previous reports demonstrating a role for cGAMP transfer in activating NK-cells[16]. In the 4T1 model, *Enpp1*-KO metastatic lesions exhibited significant infiltration by CD45+ cells and a ~3-5-fold enrichment with CD8+ T-cells compared to wildtype counterparts (**Fig. 2E-F**). Flow cytometry-based immune profiling of dissociated lungs revealed a significant increase in CD45+ cells, CD4+ T-cells as well as granulocytic CD11b+Ly6G+ cells as compared to controls (**Fig. 2G and Extended Data Fig. 4C**). There was no overall enrichment for CD8+ T-cells in the injected lungs however there was a significant increase in PD1+ subpopulations of CD3+CD8+ and CD3+CD4+ cells (**Fig. 2G**). The overall preponderance of granulocytic cells was notable, given that ENPP1-KO tumors had higher levels of GM-CSF as measured using ELISA-based assays (**Fig. 2G-H**). These findings suggest that granulocytic cells may play a role in restricting metastatic colonization of *Enpp1*-KO cells, in line with previous reports showing an anti-tumor and pro-inflammatory effect of CD11b+Ly6G+ cells[24-26].

We then asked whether ENPP1 depletion might be used as a therapeutic vulnerability to sensitize otherwise resistant chromosomally unstable tumors to immune checkpoint blockade (ICB). Interestingly, ENPP1 mRNA expression was significantly higher in 4T1 cells compared to CT26 (**Fig. 3A**), in line with the latter being considered responsive to ICB in contrast to the highly resistant 4T1 model[18,27]. We postulated that *Enpp1* knockout would render 4T1 tumors responsive to ICB whereas its overexpression would confer resistance to CT26 tumors. Luciferase-expressing 4T1 cells were orthotopically transplanted into the mammary fat pad of BALB/c mice and primary tumor growth were assessed over the span of 25 days (**Fig. 3B and Extended Data Fig. 5A-B**). Animals were treated with combined ICB (anti-PD1 and anti-CTLA4) starting at day 6 after tumor cell inoculation for 4 doses followed by maintenance aCTLA4 treatment every 3 days. *Enpp1*-KO tumors exhibited a profound response to combined ICB when compared to wildtype counterparts, leading to significantly prolonged survival (**Fig. 3C-D**). To test if overexpression of ENPP1 would confer treatment resistance in otherwise sensitive CT26 tumors, we expressed eGFP or eGFP-ENPP1 in tail vein-injected CT26 cells (**Fig. 3B and Extended Data Fig. 5C**). Mice were treated with combined ICB starting at day 6 for a total of 5 doses. Strikingly, not only did eGFP-ENPP1 expression lead to increased metastasis and reduced survival of isotype control-treated mice, it also rendered this model completely resistant to combined ICB (**Fig. 3E-F**). Conversely, eGFP-expressing CT26 tumors were responsive to combined ICB with 60% of animals surviving for over 90 days, supporting a role for ENPP1 in metastasis and immune evasion of chromosomally unstable tumors.

We next sought to interrogate the role of ENPP1 in human cancers. We analyzed *ENPP1* mRNA expression across the TCGA, two independent sarcoma cohorts, and in tumor-derived organoids. We probed ENPP1 protein expression in three independent breast cancer cohorts, including two estrogen-receptor-negative (ER-) cohorts (n = 223 and 91) and one estrogen receptor-positive (ER+) cohort (n = 115). Finally, we evaluated ENPP1 expression in mucosal melanoma primary and meta-

static tumors (n = 24). Unlike cutaneous melanoma, mucosal melanoma is characterized by elevated CIN, reduced tumor mutational burden, and increased resistance to immune checkpoint blockade[28,29].

ENPP1 mRNA expression was highly variable across cancer types, with highest expression levels observed in sarcomas, liver, breast, and thyroid cancers (**Extended Data Fig. 6A**). Elevated *ENPP1* mRNA was associated with reduced overall survival in multiple tumor types including breast cancer, irrespective of the hormone receptor status (**Extended Data Fig. 6B-D**). In line with these findings, we found ENPP1 mRNA levels to be significantly higher in organoids derived from human metastatic tumors compared to those originating from primary tumors (**Extended Data Fig. 7A**). This was also validated in mucosal melanomas, where metastases displayed increased cancer cell-specific ENPP1 staining intensity (**Extended Data Fig. 7B**). Tumor cell-intrinsic ENPP1 protein expression was most remarkable in lymph-node metastases where cancer cell clusters exhibited strong ENPP1 expression in an otherwise immune-cell replete microenvironment (**Extended Data Fig. 7C-D**). In primary breast tumors, we observed three distinct patterns of ENPP1 protein expression: tumor-cell-dominant, stroma-dominant, and negative (**Fig. 4A and Extended Data Fig. 7E**). Overall, 64% of primary TNBCs exhibited moderate or strong ENPP1 staining in either tumor cells or the stroma – a distribution that was consistent across the two ER- cohorts – compared with 90% of ER+ tumors, which displayed enrichment for tumor-cell intrinsic expression (**Extended Data Fig. 7E**). Across all three cohorts, high ENPP1 protein expression was associated with reduced survival and increased metastasis and disease relapse (**Fig. 4B and Extended Data Fig. 7F-G**).

We next correlated ENPP1 protein levels with tumor-infiltrating lymphocytes (TILs) and CD8+ T-cell density across breast cancers and found an inverse correlation between ENPP1 IHC expression intensity and lymphocytic infiltration (**Fig. 4C-D and Extended Data Fig. 8A**). We reasoned that if ENPP1 impacts tumor immune infiltration through cGAMP degradation, then its levels would be solely relevant in tumors with high levels of cGAS. We segregated the 1,079 breast cancers found in the TCGA into four subsets based on their relative *CGAS* and *ENPP1* expression levels and used the CIBERSORT method to infer the prevalence of immune cell subsets from tissue expression profiles[30]. Expectedly, *ENPP1* expression was minimally associated with the immune cell fraction in tumors with low *CGAS* expression, whereas in those with high *CGAS* mRNA, it was inversely correlated with the overall leukocyte fraction as well as with the proportion of CD8+ T-cells, CD4+ T-cells, and pro-inflammatory macrophages in tumors with elevated *CGAS* mRNA (**Extended Data Fig. 8C**). Interestingly, PD-L1 expression had a similar pattern, with the highest levels seen in tumors with high *CGAS* and low *ENPP1* expression. Gene Set Enrichment Analysis (GSEA) comparing $cGAS^{high}ENPP1^{high}$ to $cGAS^{high}ENPP1^{low}$ breast tumors revealed upregulation of inflammatory pathways related to allograft rejection, type I interferon, and interferon-γ-associated responses in the latter subset of tumors (**Extended Data Fig. 8D**). These findings suggest that ENPP1-to-cGAS ratio might be more predictive of tumor immune infiltration compared to *ENPP1* expression levels alone. We orthogonally validated this assumption in sarcomas and mucosal melanoma tumors. In sarcomas, *ENPP1*-to-*CGAS* expression ratio was more strongly associated with the cytotoxic lymphocyte score compared with ENPP1 expression levels alone (**Extended Data Fig. 8E**). In mucosal melanomas, tumors with numerous cGAS-positive micronuclei and low ENPP1 expression exhibited increased CD8+ T-cell density, whereas those with elevated ENPP1 expression in the setting of widespread cGAS-positive micronuclei exhibited significantly reduced CD8+ T-cell infiltration (**Extended Data Fig. 9A-C**).

In line with its role modulating tumor immune responses, we found that ENPP1 expression within a given cancer type negatively correlates with its overall response rate to anti-PD1/PD-L1 therapy[31]. This inverse association was again restricted to tumor types characterized by elevated levels of cGAS expression (**Fig. 4E and Extended Data Fig. 9D**). We next analyzed the mRNA expression levels of cGAS and ENPP1 in 228 bladder cancers treated with anti-PD-L1 (aPD-L1) therapy[32]. There was an overall positive correlation between *CGAS* and *ENPP1* expression and *ENPP1* levels were significantly lower in *CGAS*^{high} tumors that responded to aPD-L1 therapy. A low ENPP1-to-cGAS expression ratio was significantly correlated to tumor response across the entire cohort (**Fig. Extended Data Fig. 9E**).

Our work reveals an adaptive mechanism by which chromosomally unstable tumours co-opt cancer cell-intrinsic cGAS-STING signaling, arising from chronic exposure to cytosolic dsDNA, without eliciting anti-tumor immune surveillance (**Fig. 4F**). By virtue of their constant exposure to cytosolic dsDNA, chromosomally unstable cancer cells must address the consequences of cGAMP leakage into the extracellular space and its potential uptake by cells in the tumor microenvironment. Through their ability to degrade cGAMP selectively in the extracellular environment, tumor cells can maintain relatively high levels of this metabolite in the intracellular compartment while minimizing paracrine STING activation in neighboring immune cells (**Fig. 4F**). Furthermore, extracellular cGAMP hydrolysis by ENPP1 generates the substrate for adenosine production converting an immune stimulatory pathway into an immune suppressive mechanism that promotes tumor progression (**Fig. 4F**)[22,23]. These findings highlight an important STING-independent function for tumor cGAS and suggests that in the presence of ENPP1, high tumor cGAS activity might in fact be paradoxically immune suppressive.

References

1. Bakhoum, S. F. & Cantley, L. C. The Multifaceted Role of Chromosomal Instability in Cancer and Its Microenvironment. *Cell* **174,** 1347–1360 (2018).
2. Burrell, R. A., McGranahan, N., Bartek, J. & Swanton, C. The causes and consequences of genetic heterogeneity in cancer evolution. *Nature* **501,** 338–345 (2013).
3. Rosenthal, R. *et al.* Neoantigen-directed immune escape in lung cancer evolution. *Nature* **567,** 479–485 (2019).
4. McGranahan, N. *et al.* Allele-Specific HLA Loss and Immune Escape in Lung Cancer Evolution. *Cell* **171,** 1259–1271.e11 (2017).
5. Chowell, D. *et al.* Patient HLA class I genotype influences cancer response to checkpoint blockade immunotherapy. *Science* (2017). doi:10.1126/science.aao4572
6. Kato, H. & Sandberg, A. A. Chromosome pulverization in human cells with micronuclei. *J. Natl. Cancer Inst.* **40,** 165–179 (1968).
7. Crasta, K. *et al.* DNA breaks and chromosome pulverization from errors in mitosis. *Nature* **482,** 53–58 (2012).
8. Hatch, E. M., Fischer, A. H., Deerinck, T. J. & Hetzer, M. W. Catastrophic nuclear envelope collapse in cancer cell micronuclei. *Cell* **154,** 47–60 (2013).
9. Bakhoum, S. F. *et al.* Chromosomal instability drives metastasis through a cytosolic DNA response. *Nature* **553,** 467–472 (2018).
10. Yang, H., Wang, H., Ren, J., Chen, Q. & Chen, Z. J. cGAS is essential for cellular senescence. *Proc. Natl. Acad. Sci. U.S.A.* **114,** E4612–E4620 (2017).
11. Mackenzie, K. J. *et al.* cGAS surveillance of micronuclei links genome instability to innate immunity. *Nature* (2017). doi:10.1038/nature23449
12. Harding, S. M. *et al.* Mitotic progression following DNA damage enables pattern recognition within micronuclei. *Nature* (2017). doi:10.1038/nature23470
13. Sun, L. *et al.* Cyclic GMP-AMP synthase is a cytosolic DNA sensor that activates the type I interferon pathway. *Science* **339,** 786–791 (2013).

14. Ishikawa, H. & Barber, G. N. STING is an endoplasmic reticulum adaptor that facilitates innate immune signalling. *Nature* **455,** 674–678 (2008).
15. Abe, T. & Barber, G. N. Cytosolic-DNA-mediated, STING-dependent proinflammatory gene induction necessitates canonical NF-κB activation through TBK1. *J. Virol.* **88,** 5328–5341 (2014).
16. Marcus, A. *et al.* Tumor-Derived cGAMP Triggers a STING-Mediated Interferon Response in Non-tumor Cells to Activate the NK Cell Response. *Immunity* **49,** 754–763.e4 (2018).
17. Carozza, J. A. *et al.* 2'3'-cGAMP is an immunotransmitter produced by cancer cells and regulated by ENPP1. *BioRxiv* 539312 (2019).
18. Schadt, L. *et al.* Cancer-Cell-Intrinsic cGAS Expression Mediates Tumor Immunogenicity. *Cell Rep* **29,** 1236–1248.e7 (2019).
19. Bakhoum, S. F., Thompson, S. L., Manning, A. L. & Compton, D. A. Genome stability is ensured by temporal control of kinetochore-microtubule dynamics. *Nat. Cell Biol.* **11,** 27–35 (2009).
20. Li, L. *et al.* Hydrolysis of 2'3'-cGAMP by ENPP1 and design of nonhydrolyzable analogs. *Nat. Chem. Biol.* **10,** 1043–1048 (2014).
21. Löfgren, L., Pehrsson, S., Hägglund, G., Tjellström, H. & Nylander, S. Accurate measurement of endogenous adenosine in human blood. *PLoS ONE* **13,** e0205707 (2018).
22. Vijayan, D., Young, A., Teng, M. W. L. & Smyth, M. J. Targeting immunosuppressive adenosine in cancer. *Nat. Rev. Cancer* **17,** 709–724 (2017).
23. Stagg, J. *et al.* Anti-CD73 antibody therapy inhibits breast tumor growth and metastasis. *Proc. Natl. Acad. Sci. U.S.A.* **107,** 1547–1552 (2010).
24. Fridlender, Z. G. *et al.* Polarization of tumor-associated neutrophil phenotype by TGF-beta: "N1" versus 'N2' TAN. *Cancer Cell* **16,** 183–194 (2009).
25. Liu, Y. *et al.* CD11b+Ly6G+ cells inhibit tumor growth by suppressing IL-17 production at early stages of tumorigenesis. *Oncoimmunology* **5,** e1061175 (2016).
26. Fischer, M. A. *et al.* $CD11b^{+}$, $Ly6G^{+}$ cells produce type I interferon and exhibit tissue protective properties following peripheral virus infection. *PLoS Pathog* **7,** e1002374 (2011).
27. Kim, K. *et al.* Eradication of metastatic mouse cancers resistant to immune checkpoint blockade by suppression of myeloid-derived cells. *Proc. Natl. Acad. Sci. U.S.A.* **111,** 11774–11779 (2014).
28. Dabas, N., Byrnes, D. M., Rosa, A. M., Eller, M. S. & Grichnik, J. M. Diagnostic role of chromosomal instability in melanoma. *J Skin Cancer* **2012,** 914267 (2012).
29. D'Angelo, S. P. *et al.* Efficacy and Safety of Nivolumab Alone or in Combination With Ipilimumab in Patients With Mucosal Melanoma: A Pooled Analysis. *J. Clin. Oncol.* **35,** 226–235 (2017).
30. Newman, A. M. *et al.* Robust enumeration of cell subsets from tissue expression profiles. *Nat. Methods* **12,** 453–457 (2015).
31. Yarchoan, M., Hopkins, A. & Jaffee, E. M. Tumor Mutational Burden and Response Rate to PD-1 Inhibition. *N. Engl. J. Med.* **377,** 2500–2501 (2017).
32. Mariathasan, S. *et al.* TGFβ attenuates tumour response to PD-L1 blockade by contributing to exclusion of T cells. *Nature* **554,** 544–548 (2018).

Acknowledgements

We would like to thank Stephen McQuaid and Christine Greene (Northern Ireland Biobank) for technical support, members of the Bakhoum Laboratory (MSKCC), John Maciejowski (MSKCC), Simon Powell (MSKCC), Ashley Laughney (Weill Cornell Medicine), Mathieu Bakhoum (UCSD), and Christopher Garris (Rockefeller University) for constructive feedback. We would also like to thank the MSKCC genomics, molecule cytology, and RNAi cores.

Funding

SFB is supported by the Office Of The Director, National Institutes Of Health of the National Institutes of Health under Award Number DP5OD026395 High-Risk High-Reward Program, the Department of Defense Breast Cancer Research Breakthrough Award W81XWH- 16-1-0315 (Project: BC151244), the Burroughs Wellcome Fund Career Award for Medical Scientists, the Parker Institute for Immunotherapy at MSKCC, the Josie Robertson Foundation, and the MSKCC core grant P30-

CA008748. JSR-F is funded in part by the Breast Cancer Research Foundation. BI is supported by NIH K08CA222663, U54CA225088, Burroughs Wellcome Fund Career Award for Medical Scientists, and the Society for Immunotherapy of Cancer. EEP is supported by the Oxford Institute for Radiation Oncology, the Prostate Cancer Foundation, the American Society of Clinical Oncology and the Academy of Medical Sciences. The Northern Ireland Biobank has received funds from HSC Research Development Division of the Public Health Agency in Northern Ireland and the Friends of the Cancer Centre. JDW is supported by Swim Across America, Ludwig Cancer Research, SFB, ANS, and JDW are supported by the Nonna's Garden Foundation.

Author contributions

SFB conceived of this project and provided overall supervision. JL, MAD, ND, RKS, JK, JCM, SV, JAC, BI, EEP performed animal and in vitro cell-based experiments, PL provided critical experimental design input, WC, KL, MLN, PD, NR performed bioinformatics analysis, MH, CP, LG, TH, TM, HW, JRF, JDW, AS, MPH, MST, JAJ, EEP, performed and/or supervised pathologic analysis of tumor samples, OE, CS, BI, EEP, and SB supervised experimental work, performed data analysis and interpretation, and contributed to the writing of this manuscript.

Competing interests

SFB holds a patent related to some of the work described targeting CIN and the cGAS-STING pathway in advanced cancer. He owns equity in, receives compensation from, and serves as a consultant and the Scientific Advisory Board and Board of Directors of Volastra Therapeutics Inc. He has also consulted for Sanofi, received sponsored travel from the Prostate Cancer Foundation, and both travel and compensation from Cancer Research UK. JDW served as a consultant for Adaptive Biotech, Advaxis, Amgen, Apricity, Array BioPharma, Ascentage Pharma, Astellas, Bayer, Beigene, Bristol Myers Squibb, Celgene, Chugai, Elucida, Eli Lilly, F Star, Genentech, Imvaq, Janssen, Kleo Pharma, Kyowa Hakko Kirin, Linneaus, MedImmune, Merck, Neon Therapuetics, Northern Biologics, Ono, Polaris Pharma, Polynoma, Psioxus, Puretech, Recepta, Takara Bio, Trieza, Sellas Life Sciences, Serametrix, Surface Oncology, Syndax, and Syntalogic. He also receives research support from Bristol Myers Squibb, Medimmune, Merck Pharmaceuticals, and Genentech. He owns equity in Potenza Therapeutics, Tizona Pharmaceuticals, Adaptive Biotechnologies, Elucida, Imvaq, Beigene, Trieza, and Linneaus. He has received honoraium from Esanex. TM is a consultant for Immunos Therapeutics and Pfizer; is a co-founder with equity in IMVAQ therapeutics; receives research funding from Bristol-Myers Squibb, Surface Oncology, Kyn Therapeutics, Infinity Pharmaceuticals Inc., Peregrine Pharmaceuticals Inc., Adaptive Biotechnologies, Leap Therapeutics Inc., and Aprea; is an inventor on patent applications related to work on Oncolytic Viral therapy, Alpha Virus Based Vaccine, Neo Antigen Modeling, CD40, GITR, OX40, PD-1 and CTLA-4. KL reports speaker fees from Roche Tissue Diagnostics, travel compensation from BMS and grant income for Genetech. JSR-F has received fees for consulting for Goldman Sachs, REPARE Therapeutics and Paige.AI, and serves as an advisory board member for Roche Diagnostics, InVicro, Genentech, Paige.AI, Volition RX, REPARE Therapeutics and GRAIL. C.S. receives grant support from Pfizer, AstraZeneca, BMS, Roche-Ventana and Boehringer-Ingelheim. C.S. has consulted for Pfizer, Novartis, GlaxoSmithKline, MSD, BMS, Celgene, AstraZeneca, Illumina, Genentech, Roche-Ventana, GRAIL, Medicxi, the Sarah Cannon Research Institute and is an Advisor for Dynamo Therapeutics. C.S. is a shareholder of Apogen Biotechnologies, Epic Bioscience, GRAIL, and has stock options in and is co-founder of Achilles Therapeutics. Out-

side of the submitted work, K.L. and C.S. have a patent on indel burden and checkpoint inhibitor response pending and a patent on targeting of frameshift neoantigens for personalized immunotherapy pending. BI is a consultant for Merck & Co. Remaining authors declare no conflicts of interest.

Data Availability: Tumor DNA and RNA sequence data used in this manuscript is publicly available and cited as appropriate in the text and methods section. No new code was used in this manuscript

Figures and Figure legends

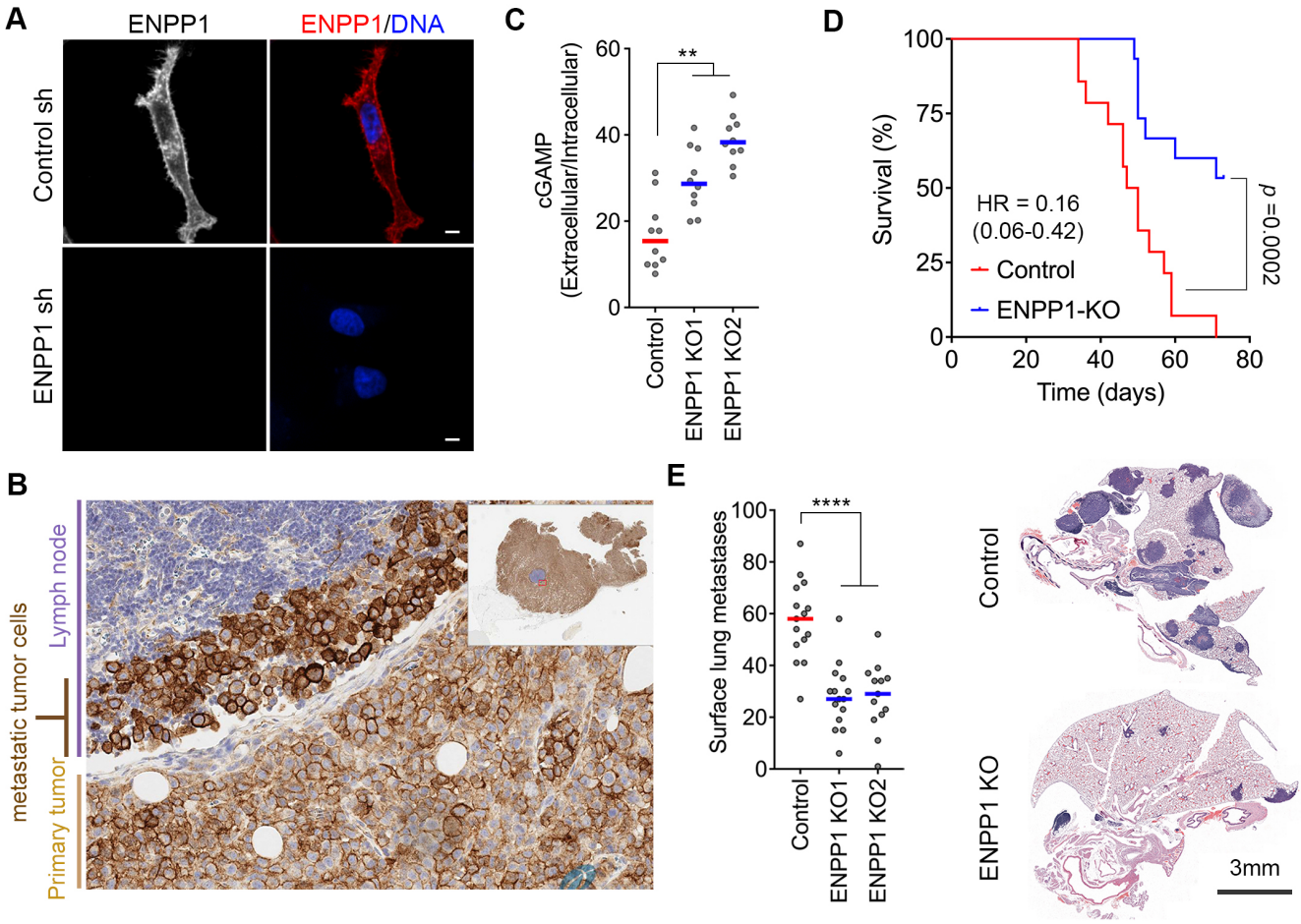

Figure 1. **ENPP1 promotes metastasis of chromosomally unstable tumors**. (A) Representative immunofluorescence images of control and ENPP1-depleted MDA-MB-231 CIN^{high} cells stained with DAPI (DNA) and anti-ENPP1 antibody, scale bar 5mm. (B) Immunohistochemistry of an orthotopically transplanted MBA-MB-231 tumor using anti-ENPP1 antibody. (C) Extracellular-to-intracellular cGAMP ratio in 4T1 cells, bars represent median, n = 10 independent experiments, ** p<0.01, two-sided Mann-Whitney test. (D) Overall survival of animals that were orthotopically transplanted by control and *Enpp1*-knockout 4T1 tumors followed by tumor resection 7 days later, n = 15 animals per condition, significance tested using log-rank test. (E) *Left,* Quantification of surface lung metastases after tail vein injection of control and *Enpp1*-knockout 4T1 cells, bars represent median, n = 13-15 animals per condition, **** p<0.0001, two-sided Mann-Whitney test. *Right*, Representative hematoxylin and eosin-stained lungs from animals injected with control and ENPP1-knockout 4T1 cells, scale bar 3mm.

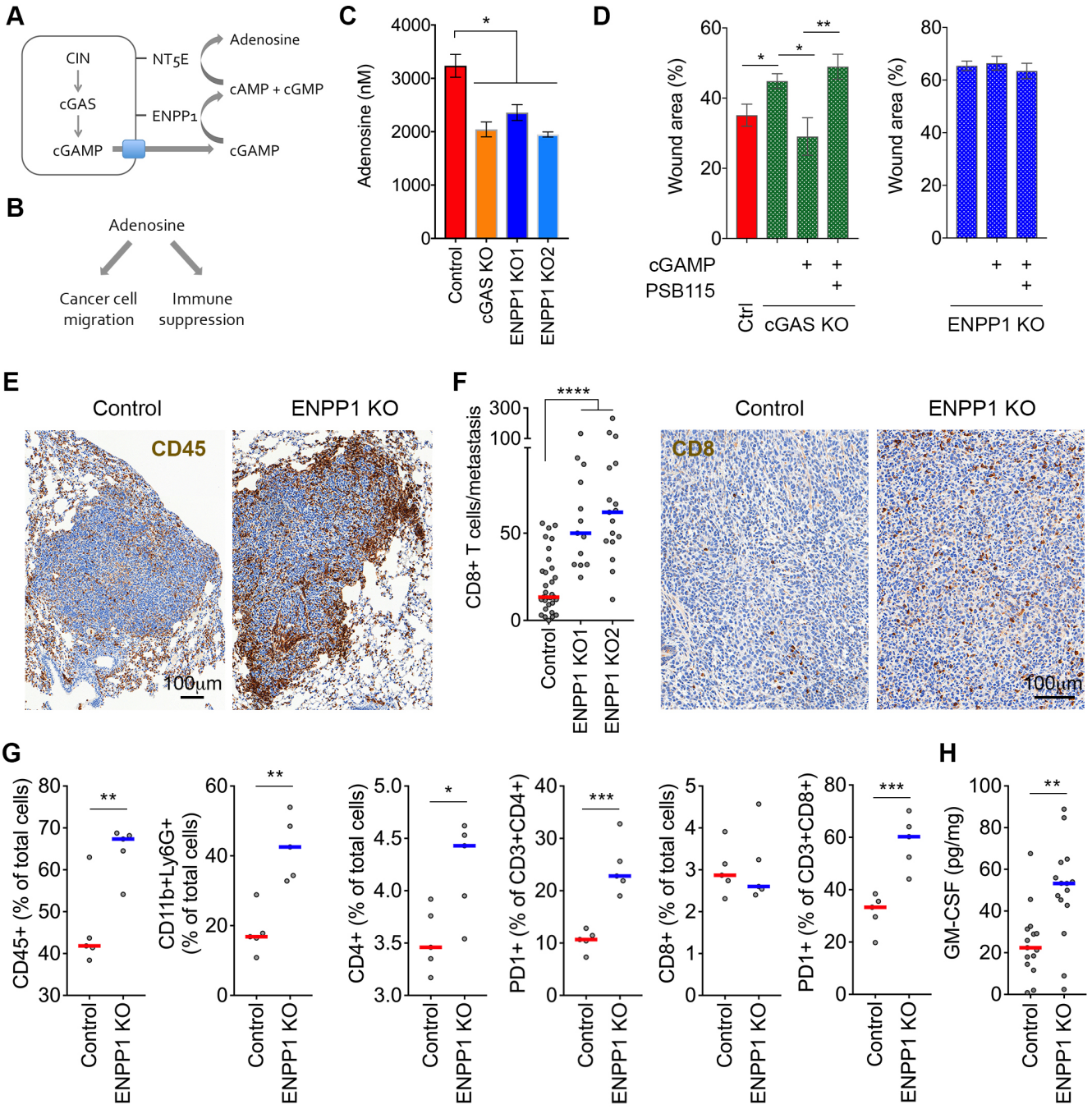

Figure 2. **ENPP1 promotes extracellular adenosine production and reduced tumor immune cell infiltration.** (A-B) Schematic showing the generation of adenosine from extracellular cGAMP hydrolysis (A) and the effects of extracellular adenosine on cancer and immune cells (B). (C) Normalized adenosine concentration (per 10^7 cells after 16 hours incubation in serum-free media) in conditioned media of control, *Cgas*-KO, *Enpp1*-KO 4T1 cells, bars represent mean ± s.e.m., n = 4 independent experiments, *p<0.05, two-sided t-test. (D) Percent wound remaining after 24 hours in control, *Cgas*-KO, and *Enpp1*-KO 4T1 cells treated with cGAMP or cGAMP and the adenosine receptor blocker, PSB115. (E) Representative immunohistochemistry (IHC) of control and ENPP1-knockout TNBC lung metastases stained using an anti-CD45 antibody. (F) The number of metastasis-infiltrating CD8+ T-cells (left) and representative IHC of control ENPP1-knockout TNBC lung metastases stained using anti-CD8 antibody (right), bars represent median, n = 13-31 metastases, **** *p*<0.0001, two-sided Mann-

Whitney test. (G) Percentage of CD45+, CD11b+Ly6G+, CD4+, and CD8+ cells out of the total cells as well as the percentage of PD1+ cells out of the CD3+CD4+ and CD3+CD8+ cells obtained from dissociated lungs after injection with control or ENPP1-knockout 4T1 cells, n = 5 animals per group. (H) GM-CSF levels measured in orthotopically transplanted control and ENPP1-knockout tumors, bars represent median, n = 15 tumors per condition, ** $p<0.01$, two-sided Mann-Whitney test.

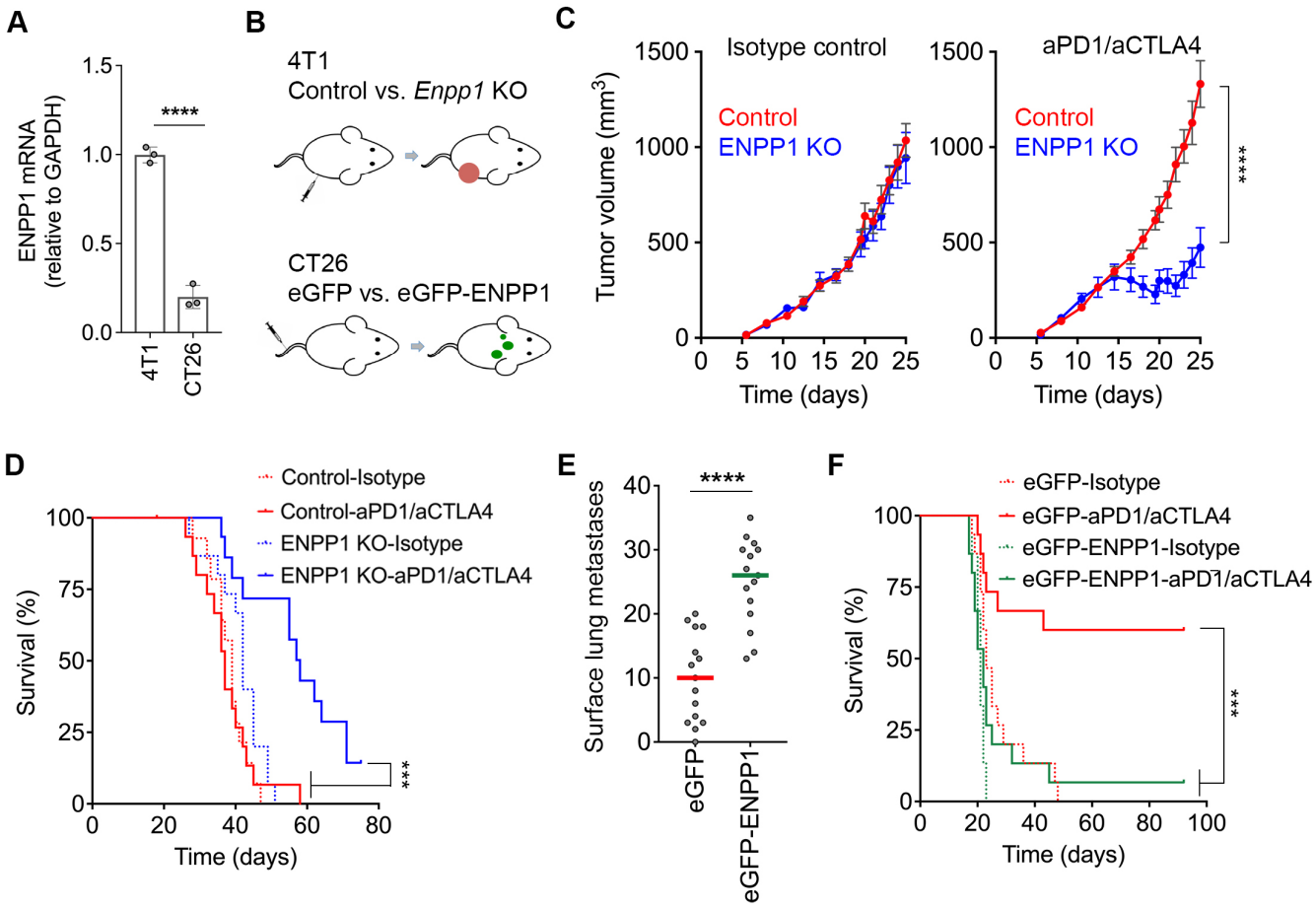

Figure 3. **ENPP1 promotes resistance to immune checkpoint blockade**. (A) Relative ENPP1 mRNA levels in 4T1 and CT26 cells. **** p<0.0001, two-tailed t-test. (B) Schematic diagram of immunotherapy experiments. (C) Growth curves of control and *Enpp1*-KO orthotopically transplanted tumors 4T1 upon treatment with combined ICB or corresponding isotype controls, data points represent mean ± s.e.m., n = 15 animals per group, ****p<0.0001, two-sided t-test. (D) Survival of animals after orthotopic transplantation with control and *Enpp1*-KO 4T1 cells treated with combined ICB or corresponding isotype controls, significance tested using log-rank test, *** p < 0.001, n = 15 animals per group. (E) Surface lung metastases after tail vein injection of eGFP and eGFP-ENPP1-expressing CT26 cells, bars represent median, n = 15 animals per condition, **** p < 0.0001, two-sided Mann-Whitney test. (F) Survival of BALB/c mice injected with eGFP or eGFP-ENPP1 expressing CT26 cells, treated with combined ICB or isotype controls, n = 15 animals per group, significance tested using log-rank test, ***p<0.001.

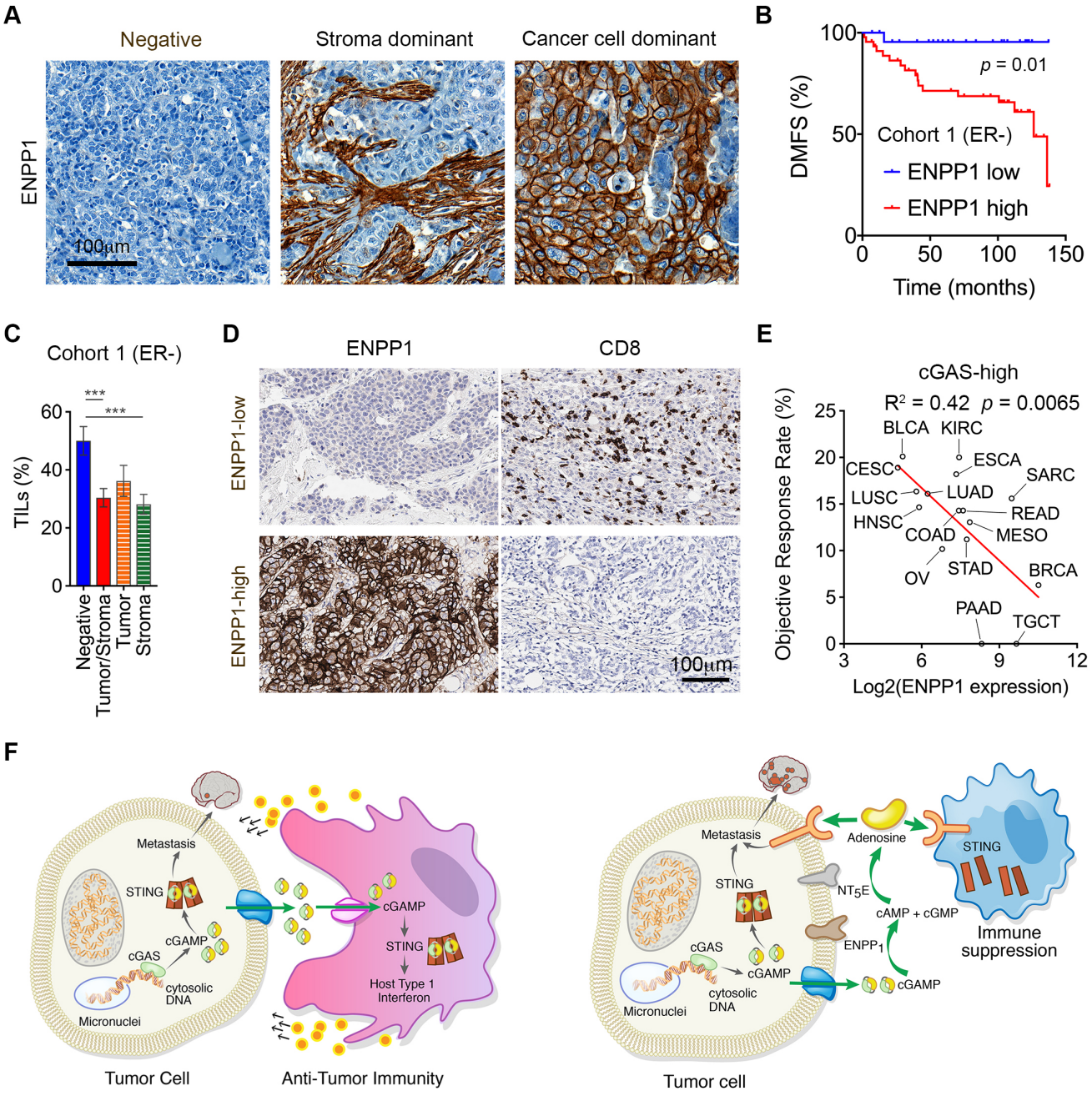

Figure 4. **ENPP1 expression is associated with metastasis and immune evasion in human cancer**. (A) Representative images of human TNBCs stained using anti-ENPP1 antibody, scale bar 100mm. (B) Distant-metastasis-free survival in patients with TNBC stratified based on their ENPP1 expression n = 69, significance tested using log-rank test. (C) Percentage of tumor-infiltrating lymphocytes (TILs) in breast tumors stratified based on their ENPP1 expression. (D) Representative images of human breast cancers stained using anti-ENPP1 or anti-CD8 antibodies. Scale bar 100mm. (E) Percent objective response rate (ORR) to anti-PD1/PD-L1 therapy as a function of ENPP1 expression by cancer type for tumor histologies with high levels of *CGAS* expression. (F) Schematic illustrating the consequence of ENPP1 activity (right) or its absence (left) on cancer metastasis and immune evasion.

Extended Data Figures and Figure legends:

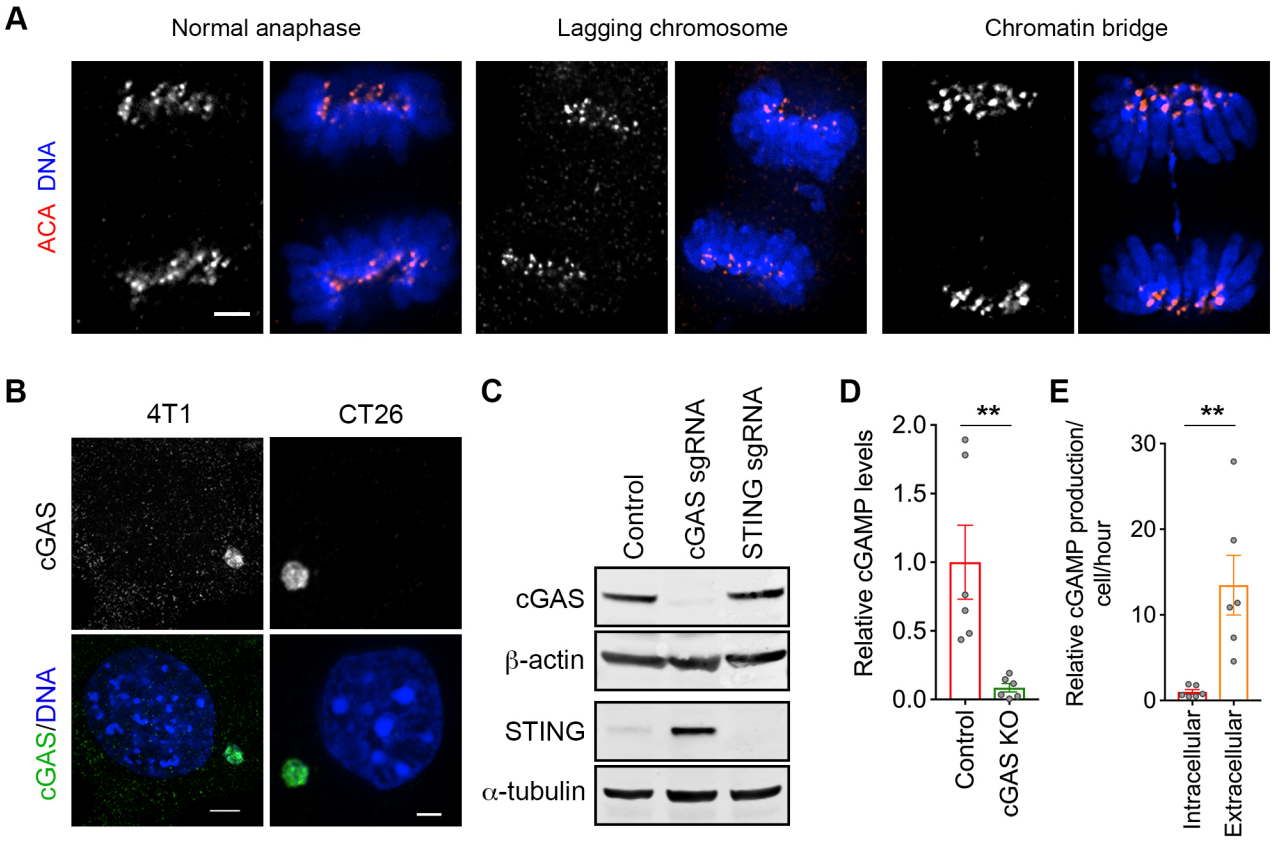

Extended Data Figure 1. (A) Representative images of 4T1 cells undergoing error-free anaphase or anaphase with evidence of chromosome missegregation, scale bar 2μm. (B) Representative image of a 4T1 cells with micronuclei stained using DAPI and anti-cGAS antibody, scale bar 2μm. (C) Immunoblots of control, cGAS-knockout, and STING-knockout 4T1 cell lysates stained using anti-STING, anti-cGAS, α-tubulin and β-actin antibodies. (D) cGAMP levels in cell lysates of 4T1 cells incubated in serum-free media for 24 hour. cAGMP levels were normalized for cell number (E) Relative intracellular and extracellular cGAMP production in 4T1 cells. Bars represent mean ± s.e.m. n = 6 independent experiments ** p<0.01, two-sided t-test.

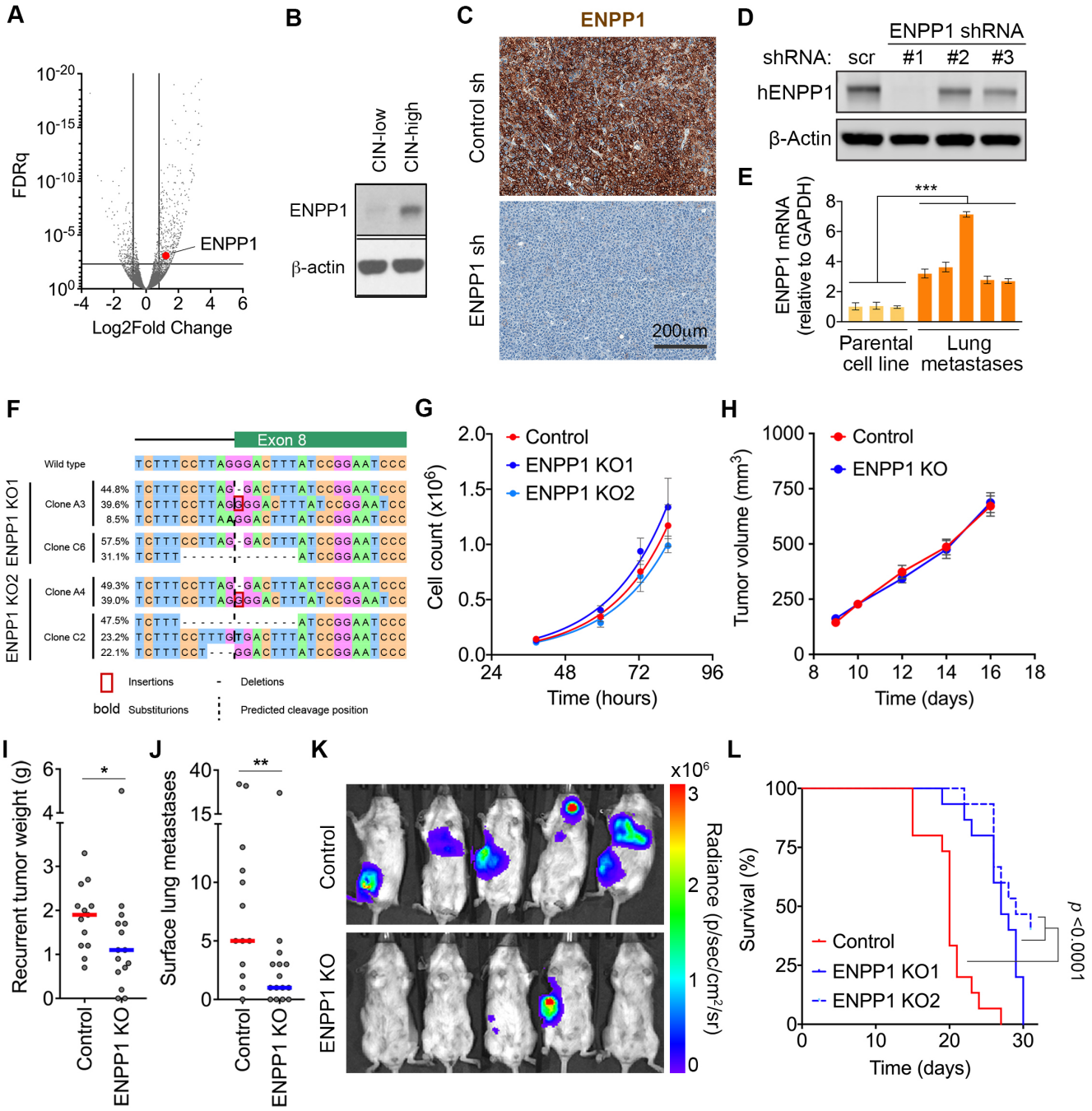

Extended Data Figure 2. (A) Volcano plot showing differentially expressed genes between MDA-MB-231 cells expressing MCAK or Kif2b (CIN^{low}) or dominant-negative MCAK (CIN^{high}). (B) Immunoblots of CIN^{low} and CIN^{high} cell lysates stained with anti-ENPP1 and anti-b-actin antibodies. (C) Representative immunohistochemistry (IHC) images of control and ENPP1-depleted orthotopically transplanted human TNBCs stained using anti-ENPP1 antibody, scale bar 200mm. (D) Immunoblots of control and ENPP1-depleted CIN^{high} MDA-MB-231 cell lysates stained using anti-ENPP1 and anti-β-actin antibody. (E) ENPP1 mRNA levels in 4T1 cells as well as cells derived from lung metastases. ***$p < 0.001$, two-tailed t-test. (F) Sequence of 4T1 single-cell derived clones showing successful ENPP1 knockout and absence of wildtype allele. (G) Proliferation of control and *Enpp1*-knockout 4T1 cells over time. (H) Volume of orthotopically transplanted control and ENPP1-knockout tumors over time. Data points represent average ± s.e.m. (I-J) Recurrent primary tumor weight (I) and surface lung metasta-

ses (J) after resection of control or *Enpp1*-knockout primary tumor resection, bars represent median, * $p<0.05$, ** $p<0.01$, two-sided Mann-Whitney test. (K) Representative bioluminescence images of BALB/c mice 35 days after orthotopic transplantation with control and *Enpp1*-KO 4T1 tumors followed by tumor resection on day 7. (L) Overall survival of animals injected by control, *Tmem173*-knockout, or *Enpp1* and *Tmem173* double-knockout 4T1 cells, n = 15 animals per condition, significance tested using log-rank test.

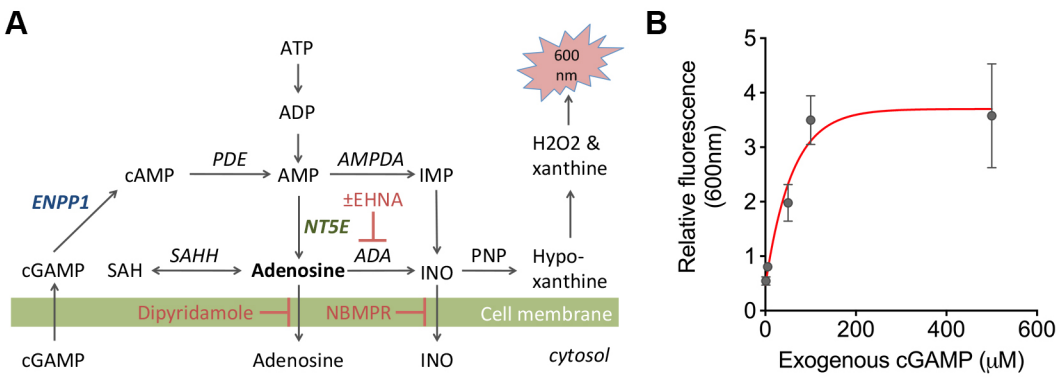

Extended Data Figure 3. (A) Schematic of extracellular adenosine metabolism illustrating an indirect fluorescence-based method of quantifying extracellular adenosine production. By subtracting fluorescence measurements obtained from media containing adenosine deaminase inhibitor, PSB115, from media without the inhibitor, we are able to quantify the amounts of downstream products arising from extracellular adenosine degradation. (B) Relative fluorescence intensity at 600 nm with and without the addition of PSB115 in the presence of increasing amounts of exogenous cGAMP.

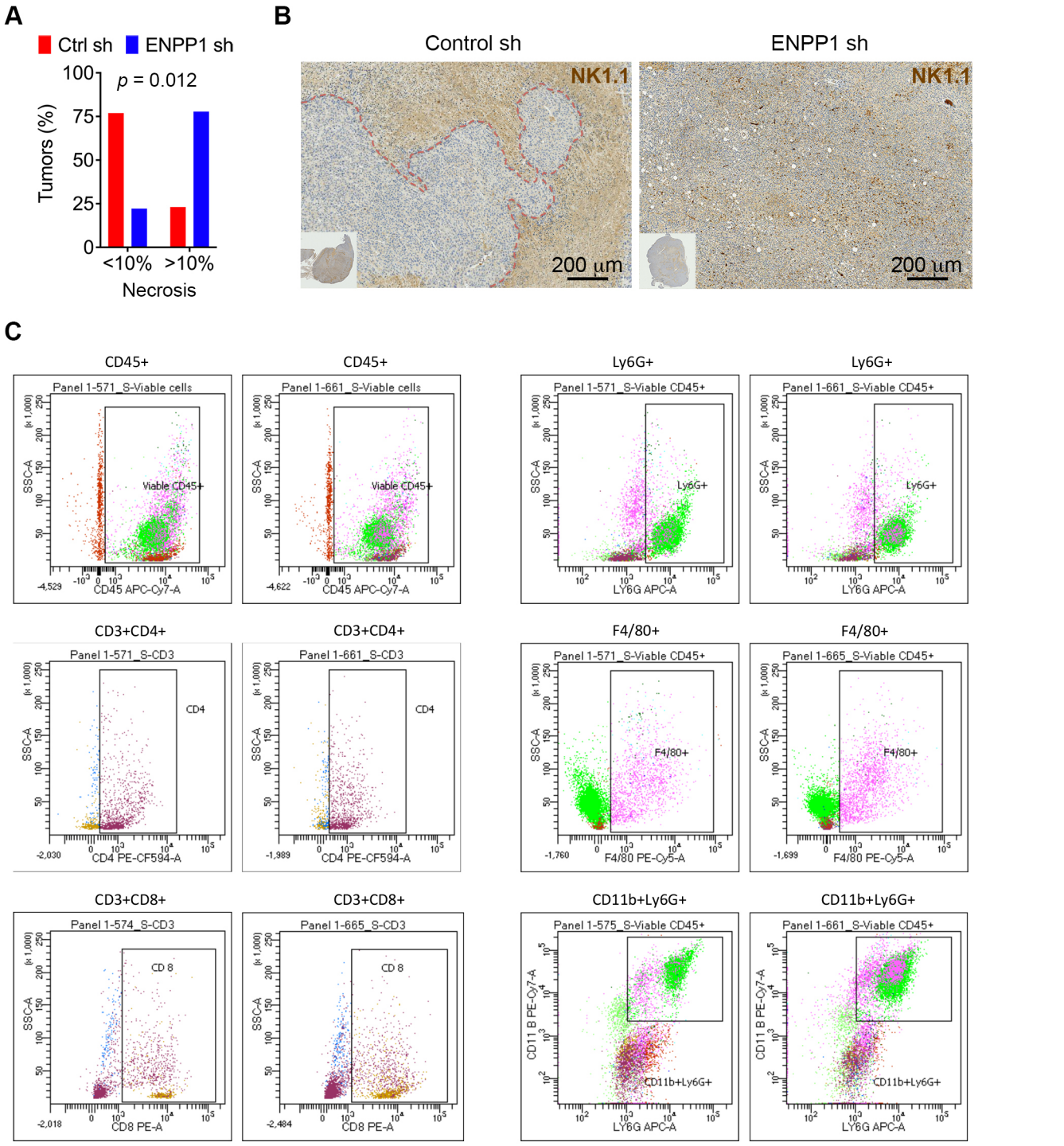

Extended Data Figure 4. (A) Semi-quantitative measurement of tumor necrosis in control and ENPP1-depleted human TNBC xenografts. (B) Representative IHC images of control and ENPP1-depleted TNBC xenografts stained using NK1.1 (to stain NK-cells), scale bar 200mm. (C) FACS gating scheme for experiments shown in **Fig. 2G**.

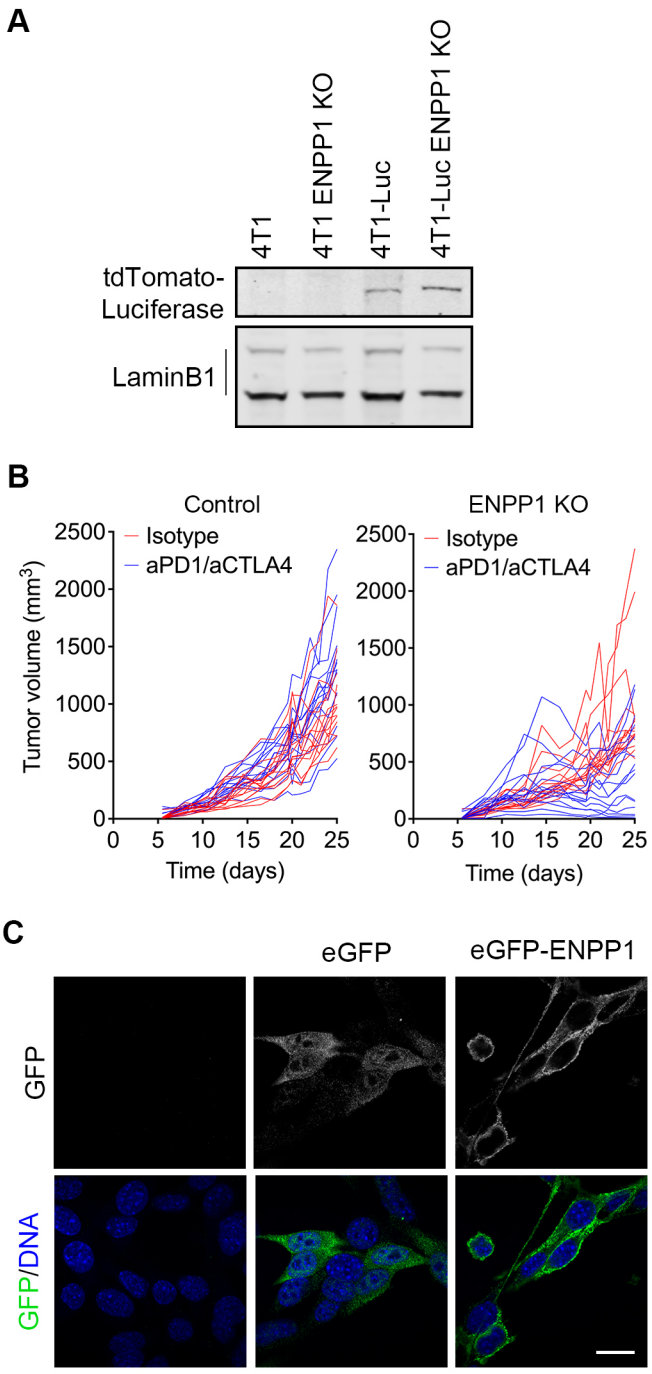

Extended Data Figure 5. (A) Immunoblots of control and luciferase expressing wildtype or *Enpp1*-KO 4T1 cells stained using anti-tdTomato-Luciferase and Lamin B1 antibodies (B) Spider plots showing growth of orthotopically transplanted control and ENPP1-KO 4T1 tumors treated with combined ICB or isotype control antibodies. (C) Representative immunofluorescence images of control, eGFP-expressing, and eGFP-ENPP1 expressing CT26 cells stained using DAPI (DNA), scale bar 10μm.

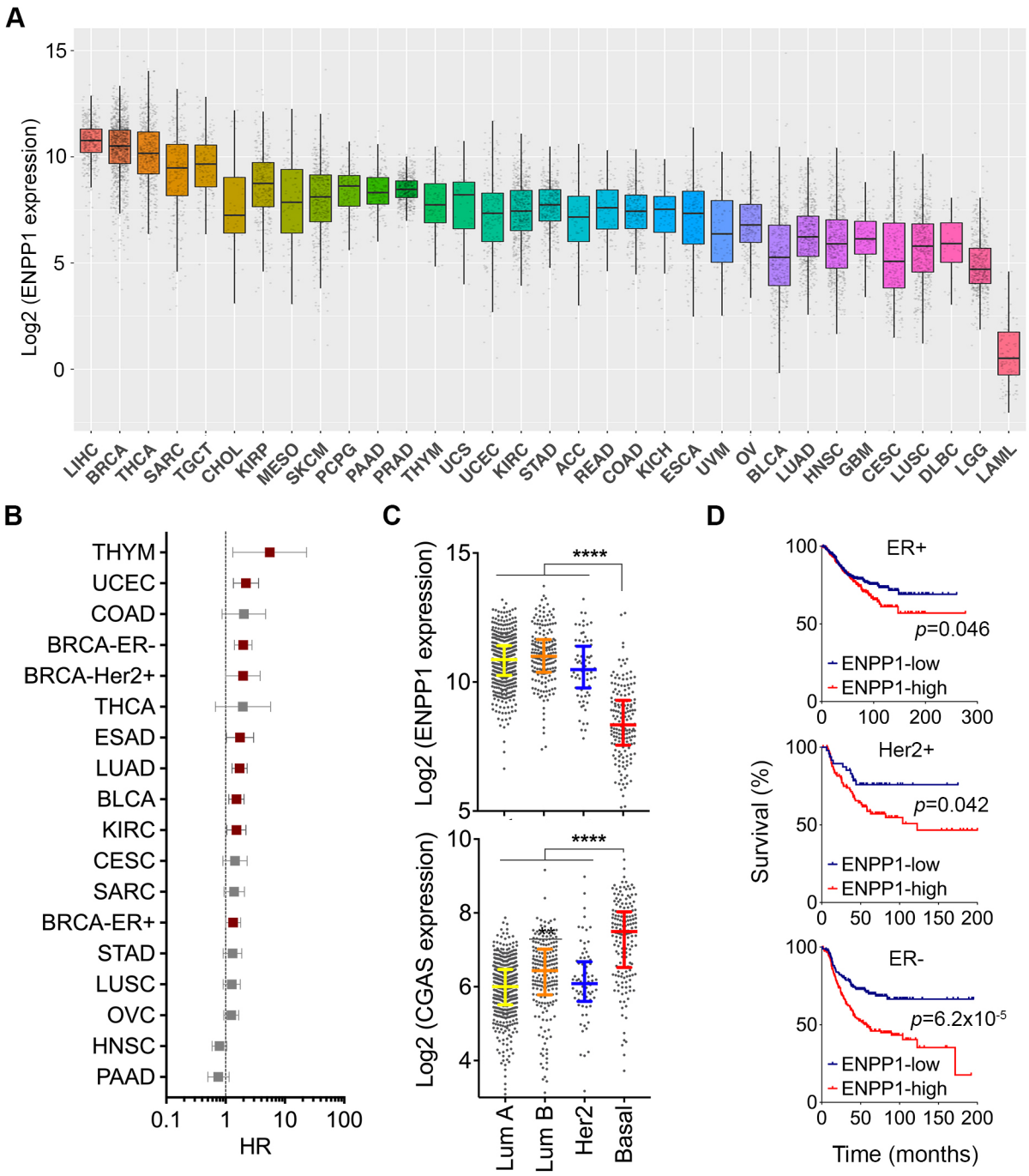

Extended Data Figure 6. (A) ENPP1 mRNA levels across human cancer types found in the TCGA database. (B) Hazard ratio for death of patients stratified by tumor ENPP1 median expression values. Data points represent HR ± 95% CI, red data points represent $p < 0.05$. (C) *CGAS* and *ENPP1* mRNA expression levels across breast cancer subtypes found in the TCGA, bars represent median ± interquartile range, ** $p<0.01$, **** $p<0.0001$, two-sided Mann-Whitney test. (D) Overall survival of breast cancer patients stratified by tumor receptor status and ENPP1 expression levels, significance tested using log-rank test.

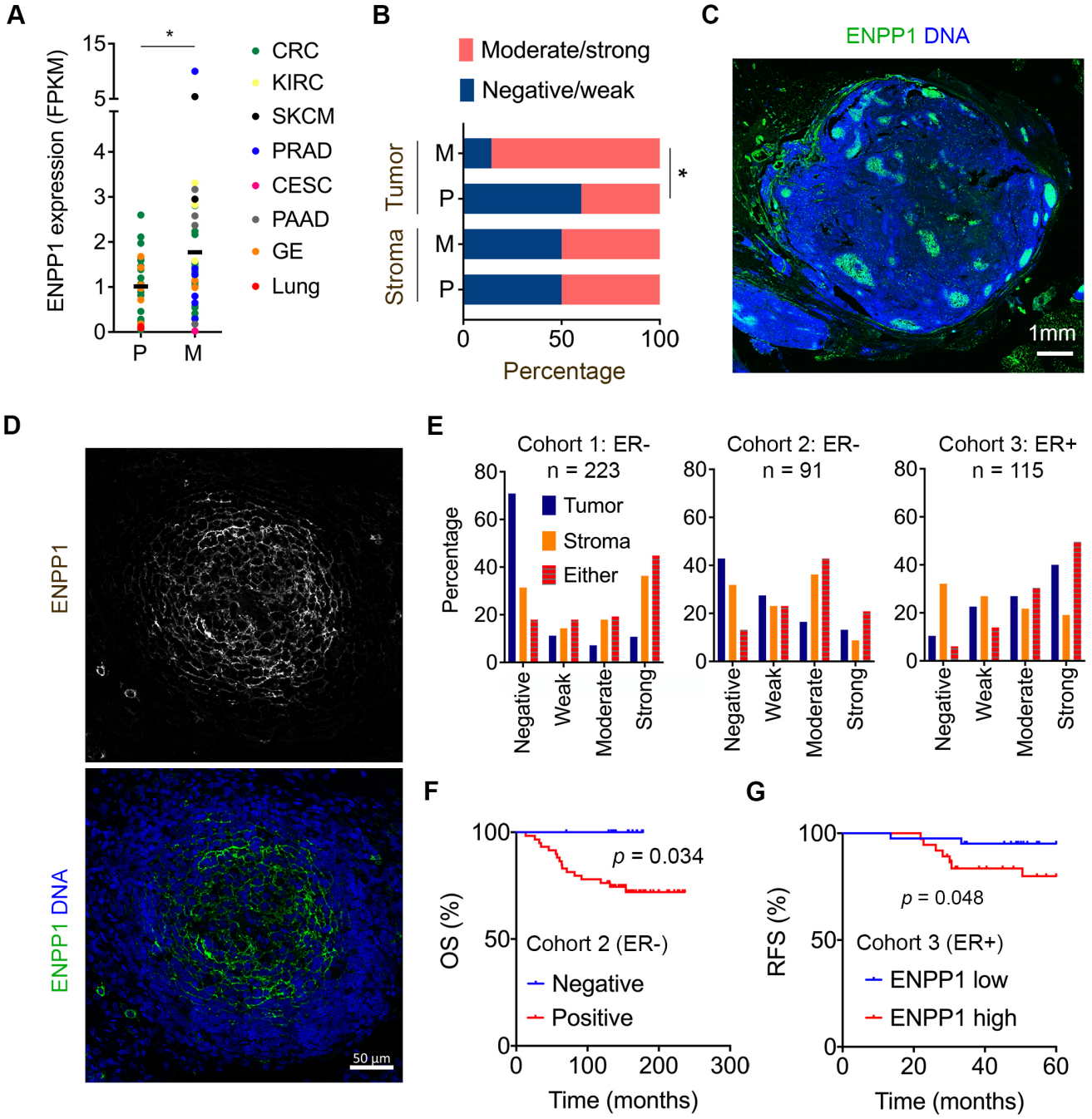

Extended Data Figure 7. (A) ENPP1 mRNA expression levels across human tumor-derived organoids. Bars represent median values, * $p < 0.05$, two-sided t-test. (B) Percentage of mucosal melanoma patients with tumor-specific or stromal specific ENPP1 staining patterns in primary as well as metastatic mucosal melanoma human tumor samples, *$p < 0.05$, χ^2-test. (C-D) Representative immunofluorescence images of low (C) and high (D) magnification images of lymph node metastases from mucosal melanoma stained using DAPI (DNA) and anti-ENPP1 antibody showing selective membrane staining of ENPP1 on metastatic cancer cells. Scale bar 1mm (C) and 50µm (D). (E) Distribution tumor samples exhibiting stroma-specific and cancer cell-specific staining patterns of ENPP1 in three independent cohorts of human breast cancer. (F-G) Overall survival (OS, F), and relapse-free survival (RFS, G) in patients with TNBC (F) or ER+ breast cancer (G) stratified based on their ENPP1 expression n = 73 (F), and 78 (G) patients, significance tested using log-rank test.

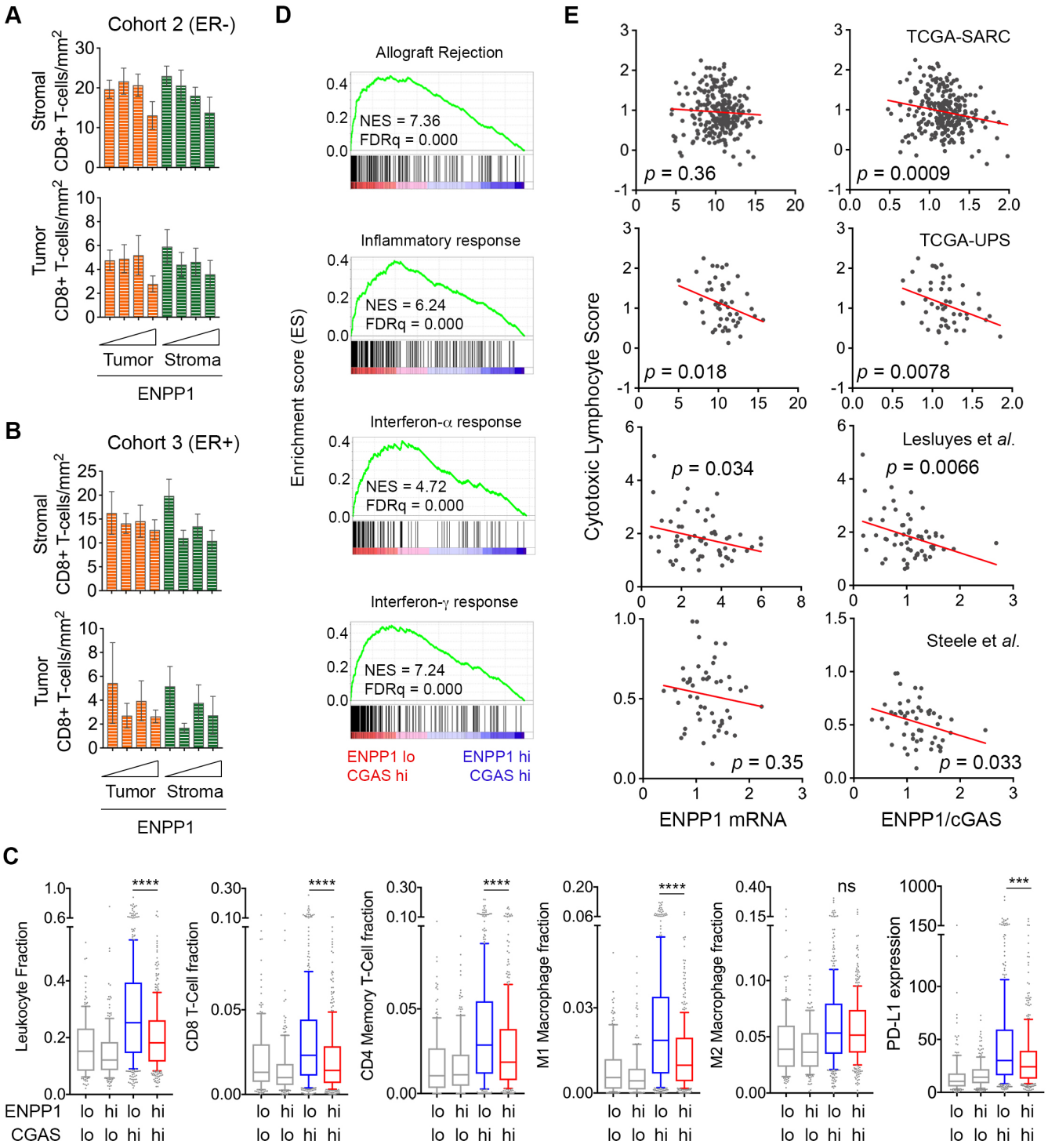

Extended Data Figure 8. (A-B) Percentage of tumor or stromal CD8+ T-cells two independent human breast cancer cohorts stratified based on their tumor and stromal ENPP1 expression. (C) Tumor immune infiltration inferred using the CIBERSORT method on breast tumors found in the TCGA, box plots represent median, lower and upper quartiles, error bars represent 10th and 90th percentiles, n = 1079 tumors, **** p<0.0001, two-sided Mann-Whitney test. (D) Gene-set enrichment plots comparing cGAS^{high}-ENPP1-^{high} and cGAS-^{high}ENPP1-^{low} human breast tumors showing upregulation of inflammation related

gene sets in ENPP1-low tumors. (E) Correlation between cytotoxic lymphocyte score and either ENPP1 levels or the ratio of ENPP1-to-cGAS mRNA levels in 3 independent sarcoma datasets.

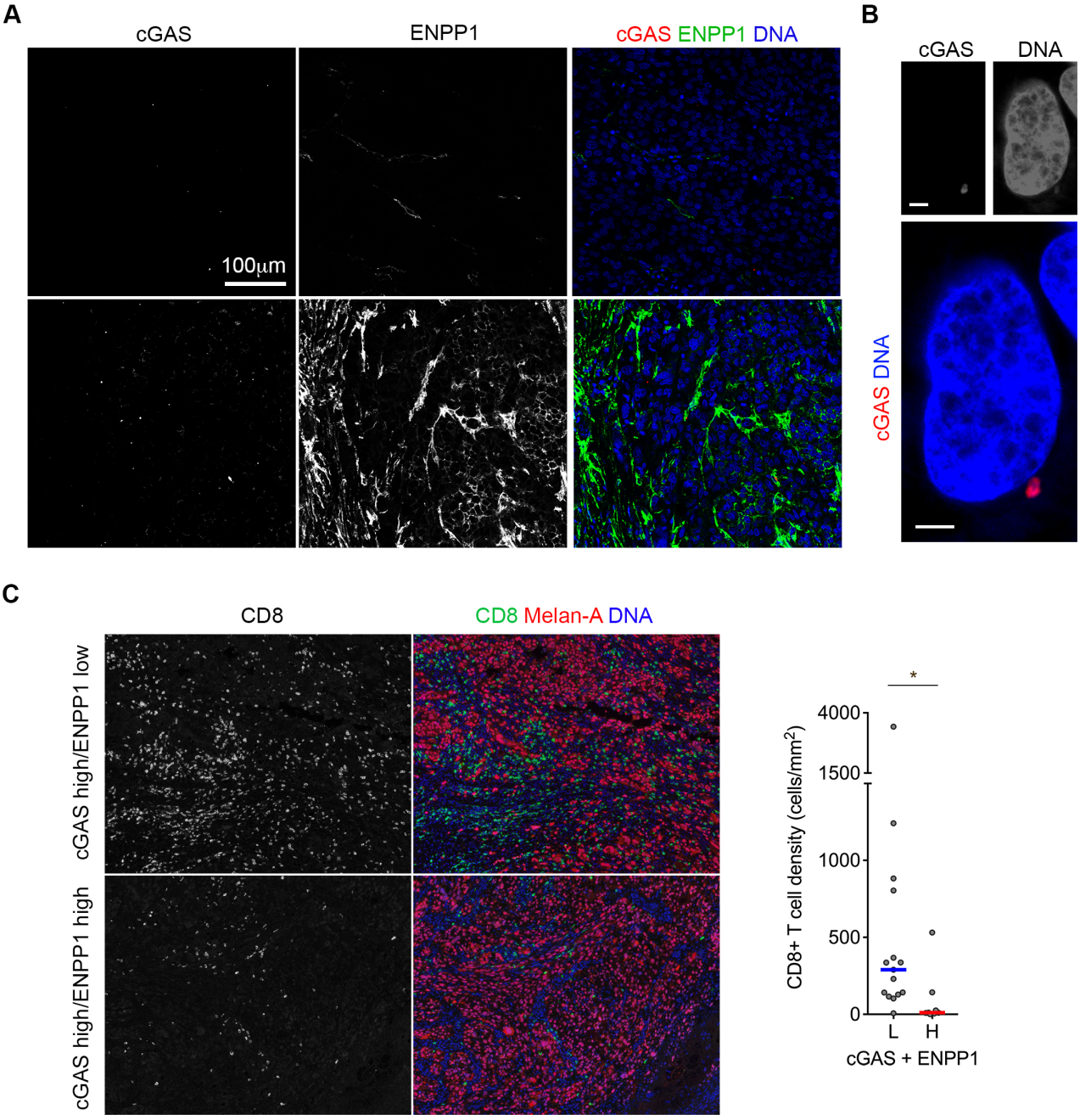
A
cGAS
ENPP1
cGAS ENPP1 DNA
100μm
B
cGAS
DNA
cGAS DNA
C
CD8
CD8 Melan-A DNA
cGAS high/ENPP1 low
cGAS high/ENPP1 high
CD8+ T cell density (cells/mm2)
4000
1500
1000
500
0
*
L
H
cGAS + ENPP1
D
cGAS-low
Objective Response Rate (%)
40
30
20
10
0
R2 = 0.02
p = 0.71
SKCM
CHOL
LIHC
UCEC
GBM
ACC
THCA
UVM
PRAD
3
6
9
12
Log2(ENPP1 expression)
E
ENPP1 expression
100
10
1
0.1
****
lo
hi
cGAS
ENPP1/cGAS expression
10
1
0.1
*
No
Yes
Response
cGAS low
ns
cGAS high
*

Extended Data Figure 9. (A) Representative immunofluorescence images of mucosal melanoma samples stained for using DAPI (DNA), anti-cGAS antibody, and anti-ENPP1 antibody, sale bar 100mm. (B) A representative high-resolution immunofluorescence image of a mucosal melanoma sample stained using DAPI (DNA) or anti-cGAS antibody showing cGAS localization to micronuclei. Scale bar 2μm. (C) *Left*, Representative multispectral immunofluorescence images of mucosal melanoma samples stained using DAPI (DNA), anti-CD8, and anti-Melan A antibodies. *Right*, CD8+ T-cell density as a function of combined cGAS and ENPP1 staining intensity in mucosal melanoma samples. Scale bar 100 μm. Bars represent median, **p*<0.05 two-sided Mann-Whitney test. (D) Percent objective response rate (ORR) to anti-PD1/PD-L1 therapy by cancer type in tumor histologies with low levels of *CGAS* expression. (E) ENPP1 and cGAS mRNA expression levels of in bladder tumors stratified by response to ICB. Bars represent median ± interquartile range, * *p*<0.05, **** *p*<0.0001, two-sided Mann-Whitney test.

Supplementary Information for

Metastasis and immune evasion from extracellular cGAMP hydrolysis

Jun Li[1,2,*], Mercedes A. Duran[1,2,*], Ninjit Dhanota[1,2], Walid Chatila[1,3], John Kwon[1,2], Roshan K Sriram[4], Matthew P Humphries[5], Manuel Salto-Tellez[5,6], Jacqueline A. James[5], Matthew Hanna[7], Johannes C. Melms[8,9], Sreeram Vallabhaneni[10], Kevin Litchfield[11], M. Laura Martin[12], Princesca Dorsaint[12], Julie-Ann Cavallo[1,2], Peng Li[13], Chantal Pauli[14], Lee Gottesdiener[15], Benjamin J. DiPardo[16], Travis Hollmann[7], Taha Merghoub[1,15,18-20], Hannah Wen[7], Jorge S. Reis-Filho[7], Nadeem Riaz[2], Anusha Kalbasi[17], Neil Vasan[15,18], Jedd D. Wolchok[1,15,18-20], Olivier Elemento[12], Charles Swanton[11], Alexander N. Shoushtari[15,18], Benjamin Izar[8,9,21,$], Eileen E. Parkes[5,6,$], Samuel F. Bakhoum[1,2,#]

Corresponding author:
Samuel F. Bakhoum, M.D., Ph.D.
Human Oncology and Pathogenesis Program
Department of Radiation Oncology
Memorial Sloan Kettering Cancer Center
New York, N.Y., 10065
Email: bakhoums@mskcc.org
Phone: 212-639-5749

Materials and methods:

Cell culture: 4T1, CT26, and B16F10 cells lines were purchased from the American Type Culture Collection (ATCC) and cultured in DMEM (B16F10) or RPMI (4T1) supplemented with 10% FBS and 2 mM L-glutamine in the presence of penicillin (50 U ml^{-1}) and streptomycin (50 µg ml^{-1}). All cells were found to be negative for mycoplasma upon repeated testing.

The generation of knockout cell lines: Murine cancer cells deficient in *Cgas*, *Tmem173*, or *Enpp1* were generated by Cas9 ribonucleoprotein nucleofection using a Lonza 4D-Nucleofector and SF Cell line Kit. crRNA (IDT) sequences is listed in Supplementary Table 1. Four guides were screened per target and knockout cell lines were confirmed using immunoblotting. Antibody information used in immunoblotting experiments is listed in Supplementary Table 2. Stable knockdown of ENPP1 in MDA-MB-231 cells was achieved using shRNAs in pRRL (SGEP or SGEN) plasmids obtained from the MSKCC RNA Interference Core. Four distinct shRNA hairpins were screened per target. Targeted shRNA sequences are listed in Supplementary Table 1.

cGAMP quantification: For intracellular and extracellular cGAMP quantification in cancer cell lines, cancer cells were seeded in 15 cm culture dishes. When culture plates were 80-90% confluent, media was changed to serum free phenol red free

RPMI (Corning). Sixteen hours following media exchange, the conditioned media was removed and centrifuged at ≥ 600 x g at 4°C for 15 minutes. Supernatant was assayed directly. All the steps were performed on ice. Cells were washed with PBS twice then trypsinzed for 5 min at 37°C and cells counts were measured. Cells were then centrifuged at ≥ 600 x g at 4°C for 15 minutes. Whole cell lysates were generated by lysing the cell pellet in LP2 lysis buffer (Tris HCl pH 7.7 20 mM, NaCl 100 mM, NaF10 mM, beta-glycerophosphate 20 mM, MgCl2 5 mM, Triton X-100 0.1% (v/v), Glycerol 5% (v/v)). The homogenate was then subjected to centrifugation at 10,000 g for 15 min. cGAMP ELISA was performed according to manufacturer's protocol using DetectX® Direct 2',3'-Cyclic GAMP Enzyme Immunoassay Kit (Arbo Assay).

Immunofluorescence microscopy: Cells were fixed with ice-cold (−30 °C) methanol for 15 min (when staining for centromeres and cGAS) or 4% paraformaldehyde (when staining for ENPP1 and GFP). Subsequently, cells were permeabilized using 1% triton for 4 min. See Supplementary Table 3 for antibody information. TBS–BSA was used as a blocking agent during antibody staining. DAPI was added together with secondary antibodies. Cells were mounted with Prolong Diamond Antifade Mountant (Life Technologies, P36961).

Immunoblotting: Cells were pelleted and lysed using RIPA buffer. Protein concentration was determined using BCA protein assay and 20–30 μg total protein were loaded in each lane. Proteins were separated by gradient SDS–PAGE and transferred to PVDF or nitrocellulose membranes. See Supplementary Table 2 for antibody information. Membranes were imaged using the LI-COR Odyssey software.

ENPP1 staining of human xenografts: Immunohistochemistry for ENPP1 in human breast cancer xenografts was performed on the automated Discovery XT processor (Ventana Medical Systems) by the Molecular Cytology Core Facility at MSKCC. Briefly, after deparaffinized and tumor tissue conditioning, the antigen was retrieved using sodium citrate pH6 buffer for 30 min. Following blockage with Background Buster (Innovex), the slides were incubated with 2.5 μg/ml anti-ENPP1 antibody (Abcam ab4003 at 1:200, Supplementary Table 4) for 4 hr, and then incubated with the biotinylated secondary antibody for 30 minutes. The Streptavidin-HRP D (DABMap kit, Ventana Medical Systems) and the DAB detection kit (Ventana Medical Systems) were used to detect the signal according to the manufacturer instructions. Then the slides were counterstained with hematoxylin and were mounted with Permount mounting medium. Tumor necrosis was assessed semi quantitatively by a certified pathologist based on the cross-sectional area containing necrosis. The pathologist was blinded to tumor group allocation.

H&E staining and Immune phenotyping of lung metastases: Lungs were excised from euthanized mice and submerged in 4% PFA overnight at 4 ^{o}C and then were transferred to 70% ethanol. Tissue embedding, slide sectioning, and H&E staining were performed by the Molecular Cytology Core Facility at MSKCC. Immunohistochemistry for CD8 and CD45 staining were performed using anti-CD8a (Cell Signaling Technology #98941) and anti-CD45 (Biosciences 550539) by the Laboratory of Comparative Pathology at MSKCC. For immune profiling using flow cytometry, animals were sacrificed 18 days after tail vein injection with control and ENPP1 KO 4T1 cells. Lungs were perfused through the right ventricle with 10-15 ml of PBS. The lungs were removed, and the large airways, thymus, lymph nodes were dissected from the peripheral lung tissue. The pe-

ripheral lung tissue was minced and transferred into 50 ml falcon tubes and processed in digestion buffer by mouse tumor dissociation kit (Miltenyi), according to the manufacturer's instructions. Homogenized lungs were passed through 40-μm nylon mesh to obtain a single-cell suspension. The remaining red blood cells were lysed using BD Pharm Lyse (BD Biosciences, San Jose, CA). Cells were stained with viability dye LIVE/DEAD™ Fixable Blue Dead Cell Stain Kit (Invitrogen), followed by incubation with FcBlock (Invitrogen), and stained with a mixture of fluorochrome-conjugated antibodies (see Supplementary Table 5 for a list of antibodies, clones, fluorochromes, and manufacturers). Data were acquired on a BD LSR II flow cytometer using BD FACS Diva software (BD Biosciences); compensation and data analysis were performed using FCS express 7 software. Unstained biological controls and single-color controls were used. Cell populations were identified using sequential gating strategy (**Extended Data Fig. 4C**).

Quantitative PCR: RNA was extracted from cells with Trizol (Invitrogen #15596026). cDNA was synthesized using the RNA to cDNA EcoDry™ Premix (Double Primed) kit (Takara #639549). Real-time PCR was performed to measure the relative mRNA expression levels of ENPP1 and the control GAPDH using Luna® Universal qPCR Master Mix (NEB M3003L). The qPCR reaction and analysis were performed on a QuantStudio 6 platform (Life technology). The sequence of primers for ENPP1 is 5'-CAGTTGACAATGCCTTTGGAATG-3' and 5'-CACTCTATCACAGGAGGTCTGG-3'. The sequence for primers for GAPDH is 5'-AGGTCGGTGTGAACGGATTTG-3' and 5'-TGTAGACCATGTAGTTGAGGTCA-3'.

Adenosine measurements: 4T1 cells were seeded in 10 cm culture dishes in quadruplicates. When culture plates reached 80-90% confluence, 7 ml serum free phenol red free RPMI (Corning) with and without inhibitors (EHNA 100 μmol/L, NBMPR 100 μmol/L, Dipyridamole 40 μmol/L) was added to plates. Conditioned media was collected after 16 h incubation. Conditioned media was centrifuged at 10,000 g for 10 min at 4ºC. Cells were harvested and cell counts were recorded for back calculations. Direct quantification of adenosine in flash-frozen conditioned media was performed by Charles River Laboratories Inc. (San Francisco). Adenosine concentrations were determined by high performance liquid chromatography (HPLC) with tandem mass spectrometry (MS/MS) detection in multiple-reaction-monitoring mode (MRM). In brief, 4 μL of internal standard solution containing 10nM Adenosine-13C5 was added to 10 μL of undiluted experimental sample. 10 μL was injected into an Infinity 1290 LC system (Agilent, USA) by an automated sample injector (SIL-20AD, Shimadzu, Japan). Analytes were separated by liquid chromatography using a linear gradient of mobile phase B at a flow rate of 0.200 mL/min on a reversed phase Atlantis T3 C18 column (2.1*150 mm, 3.0 μm particle size; Waters, USA) held at a temperature of 40 °C. Mobile phase A consisted of 5mM ammonium formate in ultrapure water. Mobile phase B was Methanol. Acquisitions were achieved in the positive ionization mode using a QTrap 5500 (Applied Biosystems, USA) equipped with a Turbo Ion Spray interface. The ion spray voltage is set at 5.0 kV and the probe temperature is 500°C. The collision gas (nitrogen) pressure was kept at the Medium setting level. The following MRM transitions were used for quantification: *m/z* 268.2/136.1 for Adenosine. Data were calibrated and quantified using the Analyst™ data system (Applied Biosystems, version 1.5.2). For indirect adenosine measurements in conditioned media after cGAMP addition were performed using the adenosine assay kit (Cell Biolabs) according to a modified manufacturer's protocol: for each sample, we measured fluorescence intensity at 600nm with and without the adenosine deaminase inhibitor, EHNA (**Extended Data Fig. 3A**).

Cellular growth and migration assays: Cellular proliferation rates were assessed by seeding $5x10^4$ control or *Enpp1*-KO 4T1 cells in 6-well plates (3-4 replicates per condition). Cells were seeded in the regular RPMI medium with 10% Fetal bovine serum (FBS). About 48 hours before cells growing to form a 90% confluency monolayer, regular media were replaced with media containing indicated drugs. The working concentration of cGAMP, adenosine, and the A2B antagonist PSB115 was 5.5 μM, 5.5 μM, and 1 μM, respectively. Fresh medium was changed every 12 hours. When reaching ~ 90% confluency, cells were treated with RPMI medium containing 10 μM Mitomycin C for 1 hour. Wounds were formed using sterile P200 pipette tips. Images of the wounds were captured every 8 hours and were analyzed with a wound healing tool macro in ImageJ (http://dev.mri.cnrs.fr/projects/imagej-macros/wiki/Wound_Healing_Tool).

Animal metastasis studies: Animal experiments were performed in accordance with protocols approved by the MSKCC Institutional Animal Care and Use Committee. For survival experiments in 4T1 experiments, power analysis indicated that 15 mice per group would be sufficient to detect a difference at relative hazard ratios of <0.25 or >4.0 with 80% power and 95% confidence, given a median survival of 58 days in the control group and a total follow up period of 180 days also accounting for accidental animal death during procedures. There was no need to randomize animals. Investigators were not blinded to group allocation. For tail vein injections, $2.5x10^4$ 4T1 or 10^5 CT26 cells were injected into the tail vein of 6-7-week old BALB/c mice. Metastasis was primarily assessed through overall survival. Overall survival endpoint was met when the mice died or met the criteria for euthanasia under the IACUC protocol. Surface lung metastases were assessed at endpoint by direct visual examination after euthanasia at which points lungs were perfused and fixed in 4% paraformaldehyde (4T1 experiments) or stained using india-ink (CT26 experiments). Furthermore, lung metastasis after injection of 4T1 cells was qualitatively assessed using routine hematoxylin and eosin (H&E) staining as shown in **Fig. 4A**. Metastatic dissemination in **Extended Data Fig. 2K** was determined using bioluminescence imaging. Mice were injected with d-luciferin (150 mg kg^{-1}) and subjected to bioluminescence imaging (BLI) using tan IVIS Spectrum Xenogen instrument (Caliper Life Sciences) to image locoregional recurrence as well as distant metastases. BLI images were analyzed using Living Image Software v.2.50. For orthotopic tumor implantation, 5×10^5 4T1 cells in 50 μl PBS were mixed 1:1 with Matrigel (BD Biosciences) and injected into the fourth mammary fat pad. Only one tumor was implanted per animal. Primary tumors were surgically excised on day 7 after implantation and metastatic dissemination was assessed by monitoring overall survival or on day 30 through quantification of surface lung metastases upon euthanasia.

Analysis of ENPP1 protein expression and tumor infiltrating lymphocytes in breast tumor samples: Primary analysis of ENPP1 protein expression was performed on a tissue microarray (TMA) of comprising 226 TNBC FFPE tumor samples of which 223 had sufficient material. Samples and follow up data for cohort 1 were collected MSKCC IRB approval. There were 3 cores per tumor sample. Detailed clinical characteristics and clinical follow-up data were previously reported [1]. Immunohistochemistry for ENPP1 in breast cancer cohort 1 was performed on the automated Discovery XT processor (Ventana Medical Systems) by the Molecular Cytology Core Facility at MSKCC. Briefly, after deparaffinized and tumor tissue conditioning, the antigen was retrieved using standard CC1 (Ventana Medical Systems). Following blockage with Background Buster (Innovex), the slides were incubated with 2.5 μg/ml anti-ENPP1 antibody for 4 hr, and then incubated with the biotinylated secondary antibody for 30 minutes. The Streptavidin-HRP D (DABMap kit, Ventana Medical Systems) and the DAB detection kit

(Ventana Medical Systems) were used to detect the signal according to the manufacturer instructions. Then the slides were counterstained with hematoxylin and were mounted with Permount mounting medium. Slides of immunofluorescence and immunohistochemistry were scanned with Pannoramic Flash 250 (3DHistech, Budapest, Hungary) with 20x/0.8 NA air objective by the Molecular Cytology Core Facility at MSKCC. ENPP1 protein expression levels were performed by a board-certified breast pathologist who was blinded to other clinicopathological characteristics and outcome. ENPP1 protein expression levels were assessed manually using scores of 0 (absent), 1 (weak), 2 (moderate) and 3 (strong) for both stromal and tumor compartments. Given this analysis was performed on small core material, ENPP1 expression was considered when >1% of cells showed a given staining pattern. Distant metastasis-free survival data were collected by reviewing medical records available at MSKCC. TILs were scored according to the recommendations of the international TILs working group [2] based on the original hematoxylin and eosin-stained sections corresponding to each of the tumors present in the TMA. Tumors were stratified as having low (negative or weak) or high (moderate or strong) ENPP1 expression. Independent validation studies were performed on a tissue microarray of n = 91 estrogen receptor (ER) negative (Cohort 2) and n= 115 ER positive (Cohort 3) FFPE breast tumors identified by the Northern Ireland Biobank (NIB), previously described elsewhere [3-6]. Resected tumors were available between 1998 and 2008, with long-term follow-up data (relapse-free and overall survival) collated via the Northern Ireland Cancer Registry. Immunohistochemistry (IHC) was performed on 4 μm sections for CD8 (NIB15-0168, Office for Research Ethics Committees Northern Ireland (ORECNI) 13-NI-0149) using C8/144B, M7103, Dako at 1:50 dilution after an ER2 20 minutes retrieval, and for ENPP1 (NIB19-0301, ORECNI 13-NI-0149) using EPR22262-72, ab24538, Abcam at 1:1000 dilution. Slides were scanned on an Aperio AT2 Digital scanner at 40x. CD8+ T cell infiltration was reported as CD8+ cell density per mm^2 based on the total number of cells in each core and determined using the open-source digital pathological analysis software QuPath *v0.1.2* [7,8]. Cores with < 100 tumor cells were removed from analysis and multiple core data were averaged. Rigorous quality control steps were taken to remove necrosis or keratin, tissue folds and entrapped normal structures; this was confirmed by a second reviewer with frequent consultation following an established method. ENPP1 protein expression levels were assessed manually using scores of 0 (absent), 1 (weak), 2 (moderate) and 3 (strong) for both stromal and tumor compartments as described above. Both analyses were performed blinded to other clinicopathological characteristics and outcome. Survival analysis was restricted to tumors with low nodal disease burden (N0-1). For OS analysis, ER- tumors were stratified as either positive (n= 59) or negative (n = 15) for ENPP1 staining. Given increased expression of ENPP1 in ER+ tumors in general, tumors were stratified as either having low (negative, weak, or moderate, n = 41) or high (strong, n = 42) ENPP1 staining.

ENPP1 staining and immune profiling of mucosal melanoma samples: Immunofluorescence for ENPP1 and cGAS was performed on the automated Discovery XT processor (Ventana Medical Systems) by the Molecular Cytology Core Facility at MSKCC (Pubmed: 25826597). The procedure of deparaffinization, cell condition, antigen retrieval, and nonspecific blockages was similar as described in the immunohistochemistry section above. Instead of DAB detection kit, Tyramide-Alexa Fluor 488 (Invitrogen T20922) and Tyramide-Alexa Fluor 594 (Invitrogen T20935) were used for signal detection. cGAS and ENPP1 staining were sequentially performed with 1:200 diluted anti-cGAS and 2.5 ug/ml of anti-ENPP1 antibodies as the primary antibody. DNA was stained with 5 μg/ml of DAPI in PBS for 10 minutes. Then the slides were mounted with Mowiol mounting medium.

RNAseq analysis of TCGA tumors: RNA-seq data for human tumor samples from TCGA patients were obtained from (https://gdc.cancer.gov/about-data/publications/pancanatlas) [9-11]. The data is upper-quartile normalized RSEM for batch-corrected mRNA gene expression and is from 33 different cancer types. Overall leukocyte fractions and CIBERSORT immune fractions for the TCGA Breast Cancer (BRCA) patients were obtained from (https://gdc.cancer.gov/node/998) [12]. The absolute abundance of the CIBERSORT immune cell types was obtained by multiplying the leukocyte fraction by the CIBERSORT immune fractions. The expression values for ENNP1 and CGAS from the TCGA RNA-seq data were utilized to categorize tumors into the four groups *ENPP1*^{low}*CGAS*^{low}, *ENPP1*^{high}*CGAS*^{low}, *ENPP1*^{low}*CGAS*^{high}, and *ENPP1*^{high}*CGAS*^{high}. The median expression value per cancer type was used to categorize tumors into *ENPP1*^{low} and *ENPP1*^{high} groups. Tumors with expression values less than or equal to the median for a given cancer type were considered *ENNP1*^{low}, while tumors with expression values above the median were considered *ENPP1*^{high}. The bottom tertile expression value per cancer type was used to categorize tumors into *CGAS*^{low} and *CGAS*^{high} groups. Tumors with expression values less than or equal to the bottom tertile (<33%) of *CGAS* expression in a given cancer type were categorized as *CGAS*^{low}, while tumors with expression values greater than the bottom tertile (>33%) were categorized as *CGAS*^{high}. The Wilcoxon Rank-Sum test was used to compare the relative abundance of CIBERSORT immune cell types between different *CGAS*/*ENPP1* expression subgroups. For pathway enrichment analysis, the DESeq2 R package [13] was used to identify differentially expressed genes between the *ENPP1*^{low}*CGAS*^{high} and *ENPP1*^{high}*CGAS*^{high} groups within the TCGA BRCA cohort. The Gene Set Enrichment Assay (GSEA) method [14] was used to perform a pathway enrichment analysis between the *ENPP1*^{low}*CGAS*^{high} and *ENPP1*^{high}*CGAS*^{high} groups. A pre-ranked gene list from DESeq2 was created and sorted by the following: sign of the log fold change * -log(adjusted p-value). The sorted pre-ranked list was run in GSEA with the Hallmark gene set database that was downloaded from the Molecular Signatures Database (MSigDB) [14]. Survival analysis across TCGA tumor types were performed using KMPlot [3,5] (http://www.kmplot.com) using auto-selection for best cutoff between the 25th and 75th percentiles.

RNAseq analysis of human sarcomas: Matched clinicopathological and RNA sequencing data for samples annotated as undifferentiated pleomorphic sarcoma (UPS, also known as malignant fibrous histiocytoma) were obtained from The Cancer Genome Atlas (TCGA) Genomic Data Commons Data Portal repository in May 2018. TCGA Samples were collected retrospectively from multiple institutions following institutional review board approval, processed, molecularly characterized, and pathologically verified by the TCGA Biospecimen Core Resource at the National Cancer Institute, as previously described [7]. Raw read counts were utilized for our analysis. Two additional publicly available RNA sequencing datasets of UPS tumors were obtained for validation [9,11]. For analysis of the Steele et *al*. dataset (EGAD00001004439), we utilized previously processed data (transcripts per million). For analysis of the Lesluyes et *al*. dataset, FASTQ files (SRA accession ID SRP057793) were preprocessed with Kallisto [15] using the human genome reference GRCh38 and transcript level abundances were computed using the Bioconductor package tximport [16]. The abundance of tissue-infiltrating immune cells was estimated using transcriptome-based methods. The Microenvironment Cell Populations-counter (MCP-counter) method [17] was used to determine relative abundance of various tumor immune microenvironment constituents. Specifically, MCP-counter cytotoxic T-lymphocyte (CTL) scores were calculated from expression of seven transcripts including *CD8A* and log2-normalized. CTL

scores were validated using an orthogonal transcriptome-based method, cytolytic activity (CYT) scores [18], calculated as the geometric mean of granzyme A (*GZMA*) and perforin (*PRF1*) transcript counts.

Bladder cancer response data to anti-PD-L1 treatment: RNA sequencing data was obtained from Mariathasan et *al*. [19], a metastatic urothelial cancer anti-PD-L1 treated cohort in SRA format, and reverted back to FASTQ using bam2fastq (v1.1.0). FASTQ reads were aligned to the hg19 genome using STAR [20]. Transcript quantification was performed using RSEM with default parameters [21]. Response was defined based on radiological response as per the RECIST criteria, with "CR/PR" being classified as a responder and "SD/PD" being a non-responder. The $CGAS^{high}$ group was defined as the upper two tertiles, and $CGAS^{low}$ as the bottom tertile, of *CGAS* expression.

Animal immunotherapy experiments: To assess the role of ENPP1 in the primary tumor growth upon the immune check-point blockade (ICB), we adopted the 4T1 orthotopic mammary fat pad implantation model. First, 4T1 cells (4T1-Luc) cells and 4T1-Luc *Enpp1* knockout (KO) cells were generated by stably integrating the Lentivirus pLVX vector expressing the tdTomato-Luciferase fusion gene in the 4T1 and 4T1 *Enpp1*-KO cells, respectively. Fifteen ~7-week-old mice were used for each of the arm, including four combinations of two cell lines (4T1-Luc and 4T1-Luc ENPP1 KO) and two conditions (ICB and the isotype control treatment). 250,000 4T1-Luc cells or 4T1-Luc *Enpp1*-KO cells in PBS:Matrigel (1:1) mix were injected into the mammary fat pad of Balb/c mice. 200 μg rat anti-mouse PD1 IgG2a antibody (aPD1) and 100 μg mouse anti-mouse CTLA4 IgG2b antibody (aCTLA4) or their corresponding isotype control antibodies were delivered intraperitoneally in 100 ml of PBS to mice every 3 days starting at day 6 post implantation. After 4 doses of combined ICB, maintenance aCTLA4 treatment and the corresponding isotype control were given every 3 days. The length (L) and width (W) of the tumor were measured using calipers. The tumor size was calculated according to the following formula: $L*W^2/2$. For experiment in **Fig. 3D**, endpoint was determined when primary tumor size of 2000 mm^3. For the CT26 model, 100,000 eGFP or eGFP-ENPP1 expressing CT26 cells were delivered intravenously to 7 week-old Balb/c mice. Treatment with aPD1/aCTLA4 antibodies and their corresponding isotype control antibodies was initiated intraperitoneally starting on day 6 and given every 3 days for 5 total doses. Animals were monitored for overall survival.

REFERENCES

1. Tozbikian, G. *et al.* Mesothelin expression in triple negative breast carcinomas correlates significantly with basal-like phenotype, distant metastases and decreased survival. *PLoS ONE* **9,** e114900 (2014).
2. Salgado, R. *et al.* The evaluation of tumor-infiltrating lymphocytes (TILs) in breast cancer: recommendations by an International TILs Working Group 2014. *Annals of oncology : official journal of the European Society for Medical Oncology* **26,** 259–271 (2015).
3. Győrffy, B. *et al.* An online survival analysis tool to rapidly assess the effect of 22,277 genes on breast cancer prognosis using microarray data of 1,809 patients. *Breast Cancer Res. Treat.* **123,** 725–731 (2010).
4. Mulligan, J. M. *et al.* Identification and validation of an anthracycline/cyclophosphamide-based chemotherapy response assay in breast cancer. *J. Natl. Cancer Inst.* **106,** djt335 (2014).
5. Győrffy, B., Surowiak, P., Budczies, J. & Lanczky, A. Online survival analysis software to assess the prognostic value of biomarkers using transcriptomic data in non-small-cell lung cancer. *PLoS ONE* **8,** e82241 (2013).
6. Parkes, E. E. *et al.* Activation of STING-Dependent Innate Immune Signaling By S-Phase-Specific DNA Damage in Breast Cancer. *J. Natl. Cancer Inst.* **109,** (2017).
7. Cancer Genome Atlas Research Network. Comprehensive and Integrated Genomic Characterization of Adult Soft Tissue Sarcomas. *Cell* **171,** 950–965.e28 (2017).

8. Bankhead, P. *et al.* QuPath: Open source software for digital pathology image analysis. *Sci Rep* **7,** 16878 (2017).
9. Lesluyes, T. *et al.* RNA sequencing validation of the Complexity INdex in SARComas prognostic signature. *Eur. J. Cancer* **57,** 104–111 (2016).
10. Hoadley, K. A. *et al.* Cell-of-Origin Patterns Dominate the Molecular Classification of 10,000 Tumors from 33 Types of Cancer. *Cell* **173,** 291–304.e6 (2018).
11. Steele, C. D. *et al.* Undifferentiated Sarcomas Develop through Distinct Evolutionary Pathways. *Cancer Cell* **35,** 441–456.e8 (2019).
12. Thorsson, V. *et al.* The Immune Landscape of Cancer. *Immunity* **48,** 812–830.e14 (2018).
13. Love, M. I., Huber, W. & Anders, S. Moderated estimation of fold change and dispersion for RNA-seq data with DESeq2. *Genome Biol.* **15,** 550 (2014).
14. Subramanian, A. *et al.* Gene set enrichment analysis: a knowledge-based approach for interpreting genome-wide expression profiles. *Proc. Natl. Acad. Sci. U.S.A.* **102,** 15545–15550 (2005).
15. Bray, N. L., Pimentel, H., Melsted, P. & Pachter, L. Near-optimal probabilistic RNA-seq quantification. *Nat Biotechnol* **34,** 525–527 (2016).
16. Soneson, C., Love, M. I. & Robinson, M. D. Differential analyses for RNA-seq: transcript-level estimates improve gene-level inferences. *F1000Res* **4,** 1521 (2015).
17. Becht, E. *et al.* Estimating the population abundance of tissue-infiltrating immune and stromal cell populations using gene expression. *Genome Biol.* **17,** 218 (2016).
18. Rooney, M. S., Shukla, S. A., Wu, C. J., Getz, G. & Hacohen, N. Molecular and genetic properties of tumors associated with local immune cytolytic activity. *Cell* **160,** 48–61 (2015).
19. Mariathasan, S. *et al.* TGFβ attenuates tumour response to PD-L1 blockade by contributing to exclusion of T cells. *Nature* **554,** 544–548 (2018).
20. Dobin, A. *et al.* STAR: ultrafast universal RNA-seq aligner. *Bioinformatics* **29,** 15–21 (2013).
21. Li, B. & Dewey, C. N. RSEM: accurate transcript quantification from RNA-Seq data with or without a reference genome. *BMC Bioinformatics* **12,** 323 (2011).

Supplementary Table 1. crRNA guide sequences

Gene target	crRNA vs. shRNA	Catalog number
Enpp1	crRNA	TACAACGCAAGTTGCCACTG
Enpp1	crRNA	GATTCCGGATAAAGTCCCTA
Enpp1	crRNA	GGTGACCGCTAATCATCAGG
Enpp1	crRNA	GATTACCGTGATCTGAAATG
Enpp1	crRNA	GAAGTCTATAACTTAATGTG
Cgas	crRNA	ACGCAAAGATATCTCGGAGG
Cgas	crRNA	GCGAGGGTCCAGGAAGGAAC
ENPP1	shRNA	TTAATAATCTTCTCTTCTGCCA
ENPP1	shRNA	TTTCAATAAAAAATCATTCCAC
ENPP1	shRNA	TTAGAGACAATTATATTCCGTA
ENPP1	shRNA	TATTAAATAATTTTGAGTTGTA

Supplementary Table 2. Antibodies used in immunoblots

Antibodies against	Company	Catalog number
mouse cGAS	Cell Signaling Technology	31659
β-actin	Abcam	ab6276
STING	Cell Signaling Technology	13647
α-tubulin	Sigma-Aldrich	T9026
Lamin B1	Abcam	ab16048
human ENPP1	Abcam	ab223268
human ENPP1	Abcam	ab40003

Supplementary Table 3. Antibodies used in immunofluorescence

Antibodies against	Company	Catalog number
human ENPP1	Abcam	ab223268
human centromere proteins	Antibodies Incorporated	15-234-0001
mouse cGAS	Cell Signaling Technology	31659
GFP	Sigma-Aldrich	11814460001

Supplementary Table 4. Antibodies used in immunohistochemistry

Antibodies against	Company	Catalog number
human ENPP1	Abcam	ab40003
human ENPP1	Abcam	ab223268
CD45	BD Pharmingen	550539
CD8α	Cell Signaling Technology	98941
NK1.1	Thermo Fisher Scientific	MA1-70100
human cGAS	LifeSpan BioSciences	LS-C757990
Melan-A	Santa Cruz Biotechnology	sc-20032

Supplementary Table 5. Antibodies used in flow cytometry

Antibodies against	Company	Catalog number
CD45, APC-eFluor 780	Thermo Fisher Scientific	47-0451-82
Ly6G, APC	Thermo Fisher Scientific	17-9668-82
CD4, PE-Texas Red	Thermo Fisher Scientific	MCD0417
F4/80, PE/Cy5	BioLegend	123112
CD8, PE	Tonbo Biosciences	50-0081-U500
CD11b, PE/Cy7	Thermo Fisher Scientific	25-0112-82
CD3ε, BV785	BioLegend	100355
PD1, APC/Cy7	BioLegend	135224